

# Realistic Expanding Source Model for Invariant One-Particle Multiplicity Distributions and Two-Particle Correlations in Relativistic Heavy-Ion Collisions

Scott Chapman and J. Rayford Nix

*Theoretical Division, Los Alamos National Laboratory, Los Alamos, NM 87545, USA*

(May 1, 1996)

## Abstract

We present a realistic expanding source model with nine parameters that are necessary and sufficient to describe the main physics occurring during hydrodynamical freezeout of the excited hadronic matter produced in relativistic heavy-ion collisions. As a first test of the model, we compare it to data from central Si + Au collisions at  $p_{\text{lab}}/A = 14.6 \text{ GeV}/c$  measured in experiment E-802 at the AGS. An overall  $\chi^2$  per degree of freedom of 1.055 is achieved for a fit to 1416 data points involving invariant  $\pi^+$ ,  $\pi^-$ ,  $K^+$ , and  $K^-$  one-particle multiplicity distributions and  $\pi^+$  and  $K^+$  two-particle correlations. The 99%-confidence region of parameter space is identified, leading to one-dimensional error estimates on the nine fitted parameters and other calculated physical quantities. Three of the most important results are the freezeout temperature, longitudinal proper time, and baryon density along the symmetry axis. For these we find values of  $92.9 \pm 4.4 \text{ MeV}$ ,  $8.2 \pm 2.2 \text{ fm}/c$ , and  $0.0222^{+0.0096}_{-0.0069} \text{ fm}^{-3}$ , respectively.

PACS: 25.75.-q, 21.65.+f, 24.10.Jv, 24.10.Nz

Typeset using REVTeX

## I. INTRODUCTION

It is a widely accepted theory that if nuclear matter attains a high enough energy density, it will undergo a phase transition from normal hadronic matter into a quark-gluon plasma (QGP) [1–4]. Since the discovery of such a QGP would represent a significant advancement in the fundamental understanding of nuclear interactions, there are a number of relativistic heavy-ion experiments both currently running and being planned which hope to test this theory. Unfortunately, if a QGP is formed in the laboratory, its quick expansion and cooling will cause it to transition back into normal hadronic matter long before anything can be detected. Thus, any signals for the prior existence of a QGP will necessarily be subtle and indirect.

In order to work backwards from the final observed state of the detected hadrons to an earlier state which may or may not have included a QGP, it is necessary to use a reliable transport model. One approach which has been quite successful in the past is to treat the expanding nuclear matter as a hydrodynamical fluid. This fluid is very hot and dense immediately after the collision, but with time it expands and cools. When some criterion is met (e.g., falling below a certain temperature or density), it is assumed that the fluid “freezes out” and becomes a collection of non-interacting, free-streaming hadrons. The freezeout hypersurface is thus some three-dimensional surface which separates hydrodynamically interacting nuclear fluid from free-streaming hadrons. According to this picture, when these hadrons are observed in detectors, their distributions and correlations contain information about the temperature, expansion velocities, chemical potentials, size, and shape of the fluid during freezeout.

The purpose of this paper is to present a physically reasonable parametrization of the freezeout process, and then to find the best values for the freezeout parameters by comparing theoretical distributions and correlations to experimental data through a minimization of  $\chi^2$ . This approach is somewhat different from a standard nuclear hydrodynamical approach, in which some equation of state must be assumed in order to determine how the fluid evolves

from its initial condition to its final freezeout [5]. One problem with standard nuclear hydrodynamics is that the formidable computations involved make a minimization of  $\chi^2$  impractical, so even when the agreement with experiment is quite good, one can never be sure that the *best* point in the infinite-dimensional space of all possible initial conditions, equations of state, and freezeout criteria has been found. Our more limited goal is to tackle just the problem of determining the properties of the system during freezeout.

We begin by reviewing the Wigner-function formulation of hydrodynamical freezeout and defining nine parameters that are necessary and sufficient to properly describe the gross properties of the source during freezeout. Although in Sec. II.B we use the language of hydrodynamical evolution (e.g., rarefaction waves and cooling) to motivate our approach, it should be noted that our calculations are actually concerned only with freezeout — not with the hydrodynamical evolution which might have led to it. Section II.D then includes a short explanation of how resonance decays are taken into consideration. Once the model is defined, Sec. III outlines our general method for constructing  $\chi^2$ , determining the goodness of the fit, and estimating uncertainties in the model parameters. With these tools in hand, we compare our nine-parameter model to data from central Si + Au collisions at  $p_{\text{lab}}/A = 14.6$  GeV/ $c$ , measured in experiment E-802 at the Brookhaven Alternating Gradient Synchrotron (AGS) [6–8]. The 1416 data points used consist of invariant  $\pi^+$ ,  $\pi^-$ ,  $K^+$ , and  $K^-$  one-particle multiplicity distribution measurements as well as  $\pi^+$  and  $K^+$  two-particle correlation measurements. To our knowledge, this paper represents the first attempt to simultaneously find the best fit to one-particle distribution and three-dimensional two-particle correlation data with a single expanding source model. We found that the fits converged rapidly and consistently, yielding an overall  $\chi^2$  per degree of freedom of 1.055.

## II. DETAILS OF THE MODEL

### A. Wigner Function Formulation

The Wigner function for particles of type  $\alpha$  with spin  $J_\alpha$  coming directly from a hydrodynamical system involving a sharp three-dimensional freezeout hypersurface is [9]

$$S_\alpha^{\text{dir}}(x, p) = \frac{2J_\alpha + 1}{(2\pi)^3} \frac{p \cdot n(x)}{\exp\{[p \cdot u(x) - \mu_\alpha(x)]/T(x)\} \mp 1} , \quad (1)$$

where the  $- (+)$  sign is for bosons (fermions). The quantities  $u^\mu(x)$ ,  $T(x)$ ,  $\mu_\alpha(x)$ , and

$$n_\mu(x) = \int_\Sigma d^3\sigma_\mu(x') \delta^{(4)}(x - x') \quad (2)$$

denote the local hydrodynamical flow velocity, temperature, chemical potential, and normal-pointing freezeout hypersurface element, respectively. Throughout the paper we use units in which  $\hbar = c = k = 1$ , where  $\hbar$  is Planck's constant divided by  $2\pi$ ,  $c$  is the speed of light, and  $k$  is the Boltzmann constant (except in the figures and tables, where we reinsert  $c$ ). Integrating the direct Wigner function over spacetime generates the Cooper-Frye formula for the one-particle distribution [10]:

$$P_\alpha^{\text{dir}}(\mathbf{p}) = \int d^4x S_\alpha^{\text{dir}}(x, p) = \frac{2J_\alpha + 1}{(2\pi)^3} \int_\Sigma d^3\sigma_\mu \frac{p^\mu}{\exp[(p \cdot u(x) - \mu_\alpha(x))/T(x)] \mp 1} . \quad (3)$$

The subscript  $\Sigma$  on the integral denotes the limits to the hypersurface for a finite-sized system. Because the observed particles are on mass shell,  $P_\alpha^{\text{dir}}$  depends only on the three-vector  $\mathbf{p}$  rather than on the four-vector  $p$ .

In addition to particles coming directly from the freezeout surface, there are also some which come from the decay of resonances. The total Wigner function for particle  $\alpha$  is then comprised of two parts:

$$S_\alpha(x, p) = S_\alpha^{\text{dir}}(x, p) + S_{\text{res} \rightarrow \alpha}(x, p) , \quad (4)$$

where the second term is determined by the direct Wigner functions of the contributing resonances (see Sec. II.D). The total observed multiplicity distribution for particle  $\alpha$  is

$$P_\alpha(\mathbf{p}) = \int d^4x S_\alpha(x, p) . \quad (5)$$

The correlation function for two particles of type  $\alpha$  with momenta  $\mathbf{p}_1$  and  $\mathbf{p}_2$  can similarly be expressed in terms of the Wigner function [11–15]

$$C_\alpha(\mathbf{q}, \mathbf{K}) = 1 \pm \lambda_\alpha \frac{|\int d^4x S_\alpha(x, K) \exp(iq \cdot x)|^2}{P_\alpha(\mathbf{p}_1) P_\alpha(\mathbf{p}_2)}, \quad (6)$$

where the deviation from unity of the parameter  $\lambda_\alpha$  measures the amount of coherent production of particles of type  $\alpha$ . Although the on-shell momenta of the two particles is completely specified by the six momentum components in  $\mathbf{K} = \frac{1}{2}(\mathbf{p}_1 + \mathbf{p}_2)$  and  $\mathbf{q} = \mathbf{p}_1 - \mathbf{p}_2$ , it is nevertheless notationally convenient to make the full off-shell four-vector definitions  $K = \frac{1}{2}(p_1 + p_2)$  and  $q = p_1 - p_2$ . Since both the one-particle distribution and the two-particle correlation function are determined by the Wigner function, we need only find a suitable parametrization of this function in order to compare a hydrodynamical model to these data.

## B. Definition of the Model Parameters

Our model is applicable to nearly central collisions of ultrarelativistic nuclei. For large sets of many nearly central collisions, the data should be azimuthally symmetric, so we assume azimuthal symmetry in our model. Immediately after the collision, we assume the formation of a hot, dense source which moves with some velocity  $v_s = \tanh y_s$  relative to the lab while it expands and cools in its own rest frame. If the incoming nuclei are relativistic enough in the source frame, their strong Lorentz contraction makes their thickness in the beam ( $z$ ) direction negligible, so it should be a good approximation to assume that the collision took place on a single plane at  $t = z = 0$ . Assuming also that the longitudinal flow velocities subsequently imparted to each bit of the nuclear fluid remain constant throughout the expansion, these velocities take the simple form first suggested in [16,17], namely

$$\beta_z(\eta) = \frac{z}{t} = \tanh \eta, \quad (7)$$

where  $\eta = \tanh^{-1}(z/t)$  is the spacetime rapidity of that bit of fluid in the source frame. We will show shortly that this flow profile leads to a longitudinally boost-invariant local energy.

Unlike in the longitudinal direction, there is no initial motion in the transverse direction. After the collision, however, rarefaction waves work their way radially inward, causing the matter to accelerate transversally outward. The resulting three-dimensional expansion causes the fluid to cool until eventually a low enough temperature is reached so that the matter effectively stops interacting and “freezes out.” We consider a model in which both the temperature  $T$  and chemical potential are constant at freezeout. For the latter, we define

$$\mu_\alpha = B_\alpha \mu_b + S_\alpha \mu_s + I_\alpha \mu_i . \quad (8)$$

Here  $B_\alpha$ ,  $S_\alpha$ , and  $I_\alpha$  are the baryon, strangeness, and isospin numbers of particle type  $\alpha$ , while  $\mu_b$ ,  $\mu_s$ , and  $\mu_i$  are the corresponding chemical potentials.

Although there are many possible ways to parametrize the radial flow at freezeout, the actual profile chosen may not be nearly as important as the average transverse velocity of the profile [18]. Recent hydrodynamical studies have obtained transverse flow profiles which are relatively linear in  $\rho = \sqrt{x^2 + y^2}$  out to a certain radius, outside of which they drop off quickly [19–21]. For simplicity, we assume a linear profile, and to preserve boost-invariance, we follow [21–23] by defining it to be independent of  $z$  and  $t$  in the longitudinally comoving frame of the source. In other words, we parametrize the total flow velocity of the system in the source frame by

$$u^\mu(x) = \gamma_\rho \left( \cosh \eta, \beta_\rho \cos \phi, \beta_\rho \sin \phi, \sinh \eta \right) , \quad (9)$$

where  $\gamma_\rho = 1/\sqrt{1 - \beta_\rho^2}$ , with

$$\beta_\rho(\rho) = v_t \left( \frac{\rho}{R} \right) . \quad (10)$$

Here  $R$  is the maximum transverse radius of the source and  $v_t$  is the magnitude of the transverse velocity of the fluid at  $\rho = R$ . Note that  $\beta_\rho$  is the flow velocity in the longitudinally comoving frame, but that the transverse component of the total flow velocity in the source frame is  $\beta_\rho / \cosh \eta$ .

That the flow profile is in fact boost-invariant can be most easily seen by first rewriting the source-frame particle four-momentum in the form

$$p^\mu = ( m_t \cosh(y_p - y_s), \mathbf{p}_\perp, m_t \sinh(y_p - y_s) ) , \quad (11)$$

where  $m_t = \sqrt{E^2 - p_z^2}$  is the “transverse mass,”  $y_p = \tanh^{-1}(p_z/E)$  is the rapidity of the particle in the lab frame, and  $\mathbf{p}_\perp$  is the transverse momentum two-vector. Throughout this paper, we will use the subscript  $\perp$  to denote the vector made from the two transverse components of a four-vector. Note that the quantity

$$p \cdot u(x) = \gamma_\rho m_t \cosh[(y_p - y_s) - \eta] - \mathbf{p}_\perp \cdot \mathbf{u}_\perp(\rho) \quad (12)$$

depends on the rapidity of the particle and the spacetime rapidity of the source only through their difference. Since boosting to a frame moving with longitudinal velocity  $U$  relative to the source frame can be done by subtracting  $\tanh^{-1}(U)$  from both  $(y_p - y_s)$  and  $\eta$ , the difference of these quantities is boost invariant.

In keeping with the boost-invariant profile, we assume that freezeout along the  $\rho = 0$  symmetry axis of the source occurs at a constant proper time [17]. Due to transverse expansion effects, however, freezeout may occur sooner for matter with  $\rho \neq 0$ . These assumptions are incorporated into the following equation describing the freezeout hypersurface:

$$\frac{t^2 - z^2}{1 + \alpha_t(\rho/R)^2} = \tau_f^2 = \text{const.} , \quad (13)$$

where  $\alpha_t$  parametrizes the radial behavior of the freezeout process. At a given constant slice in  $z$ , for  $-1 < \alpha_t < 0$ , freezeout proceeds radially from outside to inside. For example, freezeout for the  $z = 0$  slice begins on the outside ( $\rho = R$ ) at time  $t = t_1 = \tau_f \sqrt{1 + \alpha_t}$  and continues until the inside ( $\rho = 0$ ) freezes out at time  $t = t_2 = \tau_f$ . The case  $\alpha_t > 0$  corresponds to the less-likely possibility of freezeout proceeding radially from the inside to the outside, while  $\alpha_t = 0$  represents a freezeout which occurs at the same time for all points with a given  $z$ . The temporal duration of freezeout for the  $z = 0$  slice is just given by

$$\Delta t(z = 0) = |t_2 - t_1| = \tau_f \left| 1 - \sqrt{1 + \alpha_t} \right| . \quad (14)$$

To derive the prefactor  $p \cdot n(x)$  for the spacelike hypersurface defined by Eq. (13), it is most convenient to use the spacelike variables  $\eta$ ,  $x$ , and  $y$ . We have [21]

$$d^3\sigma_\mu(x) = \epsilon_{\mu\nu\alpha\beta} \frac{dX^\nu}{d\eta} \frac{dX^\alpha}{dx} \frac{dX^\beta}{dy} d\eta dx dy , \quad (15)$$

where the coordinate vector on the hypersurface is given by

$$X^\mu = \left( \tau_f \sqrt{1 + \alpha_t(\rho/R)^2} \cosh \eta, x, y, \tau_f \sqrt{1 + \alpha_t(\rho/R)^2} \sinh \eta \right) . \quad (16)$$

Doing the algebra, we find

$$p \cdot d^3\sigma(x) = \tau_f \left\{ \sqrt{1 + \alpha_t(\rho/R)^2} m_t \cosh [(y_p - y_s) - \eta] - \alpha_t \mathbf{p}_\perp \cdot \mathbf{x}_\perp \tau_f / R^2 \right\} d\eta dx dy , \quad (17)$$

where  $\mathbf{x}_\perp = (x, y)$ . Again, since the only  $(y_p - y_s)$  and  $\eta$  dependencies come through the difference  $[(y_p - y_s) - \eta]$ , the above expression is longitudinally boost invariant.

Since we are interested in realistic finite systems, it is necessary to put some spacelike limits on the hypersurface. We have already mentioned the maximum transverse radius  $R$ ; we also assume the existence of a maximum longitudinal radius  $z_3 = \tau_f \sinh \eta_0$  which is achieved by the source at time  $t_3 = \tau_f \cosh \eta_0$ . Because colliding nuclei have more matter in the center ( $\rho = 0$ ) than on the outside, we take our source to be spheroidal in  $\rho$  and  $\eta$  (as opposed to cylindrical, for example). In other words, on the hypersurface  $\Sigma$ , the spacelike coordinates  $\rho$  and  $\eta$  satisfy the inequality

$$\frac{\rho^2}{R^2} + \frac{\eta^2}{\eta_0^2} \leq 1 . \quad (18)$$

Since in the above equation,  $\eta$  appears alone and not in combination with  $(y_p - y_s)$ , these limits break boost invariance. Using Eq. (2) and the definition  $\tau = \sqrt{t^2 - z^2}$ , we obtain in the source frame

$$p \cdot n(x) = \left\{ m_t \cosh [(y_p - y_s) - \eta] - \frac{\alpha_t \mathbf{p}_\perp \cdot \mathbf{x}_\perp \tau_f}{R^2 \sqrt{1 + \alpha_t(\rho/R)^2}} \right\} \times \delta \left( \tau - \tau_f \sqrt{1 + \alpha_t(\rho/R)^2} \right) \theta \left( 1 - (\rho/R)^2 - (\eta/\eta_0)^2 \right) . \quad (19)$$

The freezeout hypersurface as a function of  $t$ ,  $\rho$ , and  $z$  shown in Fig. 1 corresponds to  $R = 8.0$  fm,  $\tau_f = 8.2$  fm/ $c$ ,  $\eta_0 = 1.47$ , and  $\alpha_t = -0.86$ , which are parameters that we determine in Sec. IV.B for the reaction considered here [6–8]. As mentioned before, since



$\alpha_t$  is negative, freezeout begins on the outside at  $\rho = R$  and works its way in, reaching the center at  $t = t_2 = \tau_f$ . Figure 2 shows an illustration of the hydrodynamical fluid for seven different instances in source-frame time. The inner surfaces at each time are actually freezing out, while the outer end caps are the boundaries of fluid which will freeze out later. Since the end caps are not yet on the freezeout hypersurface, their exact shapes are not actually determined by our model and are shown only to illustrate the finite nature of the source. By time  $t = \tau_f$ , freezeout has worked its way to the center, so for later times the source becomes two separated receding fireballs of continually decreasing size.

For symmetric projectile-target collisions, the rapidity  $y_s$  of the source frame relative to the lab is given simply by the average of the projectile and target rapidities. For asymmetric collisions, however, the precise value of  $y_s$  depends on how many “participant” nucleons in each nucleus collide to form the hydrodynamical source. The center of mass of the source is just the center of mass of the incoming participants rather than the total center of mass of all of the incoming nucleons (participants + spectators). Given the masses of the incoming nuclei,  $y_s$  could be estimated either purely on geometrical grounds or it could be treated as another variable parameter to be fit to data. For the asymmetric Si + Au collisions studied in this paper, we choose the latter approach.

Although at first we considered separate incoherence parameters for pions and for kaons, we subsequently found that very good fits could be obtained by setting  $\lambda_K = 1$  and allowing only  $\lambda_\pi$  to vary as a parameter. Moreover, two of the chemical potentials,  $\mu_s$  and  $\mu_i$ , can be determined from the remaining nine parameters by imposing the constraints that the total strangeness of the sum of all particles in the source vanishes and that the total isospin per baryon is the same as that of the participants before the collision (see next subsection). The nine adjustable parameters of our model can be grouped in the following way:  $T$ ,  $\mu_b/T$ , and  $\lambda_\pi$  describe intrinsic properties of the fluid;  $R$ ,  $v_t$ , and  $\alpha_t$  describe transverse aspects of the freezeout; and  $y_s$ ,  $\eta_0$ , and  $\tau_f$  describe longitudinal and boost-invariant aspects of the freezeout.

### C. Constraint Equations

The total number of particles of type  $\alpha$  which freeze out on the hypersurface is given by

$$N_{\alpha}^{\text{dir}} = \int \frac{d^3p}{E} P_{\alpha}^{\text{dir}}(\mathbf{p}) , \quad (20)$$

where  $P_{\alpha}^{\text{dir}}$  is defined by Eq. (3). Given the numbers of each particle species, the total strangeness and isospin per baryon of the system are simply

$$\begin{aligned} S_{\text{tot}}(\mu_s, \mu_i) &= \sum_{\alpha} S_{\alpha} N_{\alpha}^{\text{dir}}(\mu_s, \mu_i) \\ \frac{I_{\text{tot}}(\mu_s, \mu_i)}{B_{\text{tot}}(\mu_s, \mu_i)} &= \frac{\sum_{\alpha} I_{\alpha} N_{\alpha}^{\text{dir}}(\mu_s, \mu_i)}{\sum_{\alpha} B_{\alpha} N_{\alpha}^{\text{dir}}(\mu_s, \mu_i)} , \end{aligned} \quad (21)$$

where we have suppressed all parameter dependencies except those of  $\mu_s$  and  $\mu_i$ . The sum in  $\alpha$  is over all mesons with masses below 900 MeV and all baryons with masses below 1410 MeV. For particles of a given mass, all of the isospin, baryon, and strangeness states are considered separately since the different chemical potential of each (see Eq. (8)) leads to a different value of  $N_{\alpha}^{\text{dir}}$ .

The initial isospin per baryon of the system depends on the number of participant protons and neutrons from each nucleus. We define the target proton number, nucleon number, and number of participants as  $Z_{\text{tar}}$ ,  $A_{\text{tar}}$ , and  $B_{\text{tar}}$ , respectively. Making similar definitions for the projectile and noting that each proton (neutron) has isospin 1/2 (−1/2), we find the total isospin of the incoming participants:

$$I|_0 = \frac{B_{\text{proj}}}{2A_{\text{proj}}} [Z_{\text{proj}} - (A_{\text{proj}} - Z_{\text{proj}})] + \frac{B_{\text{tar}}}{2A_{\text{tar}}} [Z_{\text{tar}} - (A_{\text{tar}} - Z_{\text{tar}})] . \quad (22)$$

To get the isospin per baryon of the participants, we simply divide the above equation by  $B = B_{\text{proj}} + B_{\text{tar}}$ . The quantities  $B_{\text{proj}}/B$  and  $B_{\text{tar}}/B$  can be determined by equating the incoming target and projectile momenta in the participant center-of-mass frame. Explicitly,

$$m_N B_{\text{proj}} \sinh(y_{\text{proj}} - y_s) = m_N B_{\text{tar}} \sinh(y_s - y_{\text{tar}}) , \quad (23)$$

where  $y_{\text{proj}}$  and  $y_{\text{tar}}$  are the initial projectile and target rapidities and  $m_N$  is the nucleon mass. Using this relation, it is easy to show that the initial isospin per baryon of the system is given by

$$\left. \frac{I}{B} \right|_0 = -\frac{1}{2} + \frac{(Z_{\text{proj}}/A_{\text{proj}}) \sinh(y_s - y_{\text{tar}}) + (Z_{\text{tar}}/A_{\text{tar}}) \sinh(y_{\text{proj}} - y_s)}{\sinh(y_s - y_{\text{tar}}) + \sinh(y_{\text{proj}} - y_s)}. \quad (24)$$

In general, the initial isospin per baryon depends upon the parameter  $y_s$ , but for symmetric collisions (or any collision in which  $Z_{\text{proj}}/A_{\text{proj}} = Z_{\text{tar}}/A_{\text{tar}}$ ),  $I/B|_0$  is independent of  $y_s$ .

We are now ready to write down explicitly the constraint equations for  $\mu_s$  and  $\mu_i$ :

$$\begin{aligned} S_{\text{tot}}(\mu_s, \mu_i) &= 0 \\ \frac{I_{\text{tot}}(\mu_s, \mu_i)}{B_{\text{tot}}(\mu_s, \mu_i)} &= \left. \frac{I}{B} \right|_0. \end{aligned} \quad (25)$$

For a given set of the nine remaining parameters, these equations allow one to find unique values of  $\mu_s$  and  $\mu_i$  as well as their derivatives (e.g.,  $d\mu_s/dT$ ).

Notice that the baryon number of this model reflects only the participant baryons and is not constrained to be the same as the total baryon number of the two incoming nuclei. The rationale behind this is that in many collisions there are “spectator” nucleons whose evolution is not well described by a hydrodynamically expanding source. Since these spectators may nonetheless end up in detectors, this model works best when it is used to fit only data from produced particles such as mesons and antiprotons. Of course, once the parameters have been determined from a fit to mesons, for example, it is always possible to compare the proton distribution predicted by the model with the data to get an idea of how many of the measured protons are “participants” and how many are “spectators.”

It is significant that even if only meson data are considered, it is still possible to determine the baryon chemical potential  $\mu_b$  from the relative abundances of  $K^+$ 's and  $K^-$ 's. For any system which has a positive baryon number, there are more  $\Lambda$ 's and  $\Sigma$ 's produced than  $\bar{\Lambda}$ 's and  $\bar{\Sigma}$ 's. This leads to a net negative strangeness among all of the baryons. From the constraint of Eq. (25), it follows that more  $K^+$ 's than  $K^-$ 's are produced. In other words, the difference between  $K^+$  and  $K^-$  abundances provides an indirect measurement of baryon number and hence of  $\mu_b$ .

## D. Resonance Decays

For single-generation decays, the resonance contribution to the Wigner function is given by [24,25]

$$S_{\text{res} \rightarrow \alpha}(x, p) = \sum_{\beta} \int \frac{d^3 p_{\beta}}{E_{\beta}} \int d^4 x_{\beta} \int_0^{\infty} d\tau_{\beta} \Gamma_{\beta} \exp(-\Gamma_{\beta} \tau_{\beta}) \times \delta^4 \left( x - \left[ x_{\beta} + \frac{\tau_{\beta}}{m_{\beta}} p_{\beta} \right] \right) \Phi_{\beta \rightarrow \alpha}(p_{\beta}, p) S_{\beta}^{\text{dir}}(x_{\beta}, p_{\beta}) , \quad (26)$$

where the sum in  $\beta$  is over each decay channel of each resonance that will produce a particle  $\alpha$ . The quantity  $\Phi_{\beta \rightarrow \alpha}(p_{\beta}, p)$  is the probability density that a resonance with momentum  $p_{\beta}$  will decay into a particle  $\alpha$  with momentum  $p$ . For a two-body decay  $\beta \rightarrow \alpha + X$  that is isotropic in the rest frame of the resonance,

$$\Phi_{\beta \rightarrow \alpha + X}(p_{\beta}, p) = \frac{b_{\beta}}{4\pi p_0(m_{\beta}; m_{\alpha}, m_X)} \delta \left( E_0(m_{\beta}; m_{\alpha}, m_X) - \frac{p_{\beta} \cdot p}{m_{\beta}} \right) , \quad (27)$$

where  $b_{\beta}$  is the branching ratio of the particular decay channel and

$$E_0(m_{\beta}; m_{\alpha}, m_X) = \frac{1}{2m_{\beta}} (m_{\beta}^2 + m_{\alpha}^2 - m_X^2) \\ p_0(m_{\beta}; m_{\alpha}, m_X) = \frac{1}{2m_{\beta}} \sqrt{[m_{\beta}^2 - (m_{\alpha} + m_X)^2] [m_{\beta}^2 - (m_{\alpha} - m_X)^2]} . \quad (28)$$

A three-body decay  $\beta \rightarrow \alpha + X + Y$  can be treated as a two-body decay into  $\alpha$  and a system with the combined invariant mass  $M$  of particles  $X$  and  $Y$ . Since  $M$  can vary from  $m_X + m_Y$  to  $m_{\beta} - m_{\alpha}$ , it must be integrated over with an appropriate probability density. In [24,26], this has been shown to be

$$P(M) = \frac{p_0(m_{\beta}; m_{\alpha}, M) p_0(M; m_X, m_Y)}{\int_{m_X + m_Y}^{m_{\beta} - m_{\alpha}} dM p_0(m_{\beta}; m_{\alpha}, M) p_0(M; m_X, m_Y)} . \quad (29)$$

Using this probability density, we have for three-body decays

$$\Phi_{\beta \rightarrow \alpha + X + Y}(p_{\beta}, p) = \int_{m_X + m_Y}^{m_{\beta} - m_{\alpha}} dM P(M) \Phi_{\beta \rightarrow \alpha + M}(p_{\beta}, p) . \quad (30)$$

The resonances included which contribute to the charged pion distributions are [27]

$$\begin{aligned}
\eta &\rightarrow \pi^+ + \pi^- + \pi^0 \\
\eta &\rightarrow \pi^+ + \pi^- + \gamma \\
\rho &\rightarrow \pi + \pi \\
\omega &\rightarrow \pi^+ + \pi^- + \pi^0 \\
\omega &\rightarrow \pi^+ + \pi^- \\
K^* &\rightarrow K + \pi \\
\Delta &\rightarrow N + \pi \\
\Sigma(1385) &\rightarrow \Lambda + \pi \\
\Sigma(1385) &\rightarrow \Sigma + \pi \\
\Lambda(1405) &\rightarrow \Sigma + \pi .
\end{aligned} \tag{31}$$

The  $K^*$  and  $\Delta$  resonances also contribute to the kaon and nucleon distributions, respectively.

Since the model uses separate isospin, baryon, and strangeness chemical potentials, each species of each resonance must be treated separately. For example, there are four different channels by which negative pions can be produced from delta decay:

$$\begin{aligned}
\Delta^-(I = -3/2, B = 1) &\rightarrow n + \pi^- , \quad b = 0.994 \\
\Delta^0(I = -1/2, B = 1) &\rightarrow p + \pi^- , \quad b = 0.994/3 \\
\bar{\Delta}^{--}(I = -3/2, B = -1) &\rightarrow \bar{p} + \pi^- , \quad b = 0.994 \\
\bar{\Delta}^-(I = -1/2, B = -1) &\rightarrow \bar{n} + \pi^- , \quad b = 0.994/3 .
\end{aligned} \tag{32}$$

### III. DETERMINATION OF THE PARAMETERS BY $\chi^2$ MINIMIZATION

#### A. Construction of $\chi^2$

A single point  $i$  of an experimentally measured one-particle distribution for a particle of type  $\alpha$  can be characterized by the set  $(\mathbf{p}_i, P_\alpha^i, \sigma_i^{\text{stat}})$ , where  $\sigma_i^{\text{stat}}$  is the statistical error of the measurement. There are also systematic errors associated with these measurements,

which are usually expressed in terms of a percentage of  $P_\alpha^i$  for each particle  $\alpha$ . We denote the percent systematic error by  $f_\alpha$ , so that the total error for point  $i$  is given by

$$\sigma_{\alpha,i}^{\text{tot}} = \sqrt{\sigma_i^{\text{stat}2} + (f_\alpha P_\alpha^i)^2}. \quad (33)$$

For each particle  $\alpha$ , we construct its contribution  $\chi_\alpha^2$  to the total  $\chi^2$  in the following way:

$$\chi_\alpha^2(\theta) = \sum_i \frac{[P_\alpha^i - P_\alpha(\mathbf{p}_i, \theta)]^2}{\sigma_{\alpha,i}^{\text{tot}2}}, \quad (34)$$

where  $P_\alpha(\mathbf{p}, \theta)$  is defined by Eq. (5),  $\theta$  is used to represent all of the model parameters ( $T$ ,  $v_t$ , etc.), and the sum is over all of the measured data points.

A similar contribution to  $\chi^2$  can be constructed by comparing two-particle correlation data to the corresponding model calculations. The main difference with correlation measurements is that most of the systematic errors are removed when dividing the two-particle distribution measurement in the numerator by the product of the one-particle distribution measurements in the denominator. All of the individual one- and two-particle contributions to  $\chi^2$  can be combined into an overall  $\chi^2$  of the form

$$\chi^2(\theta) = \sum_\alpha \sum_i \frac{[P_\alpha^i - P_\alpha(\mathbf{p}_i, \theta)]^2}{\sigma_i^{\text{stat}2} + (f_\alpha P_\alpha^i)^2} + \sum_\beta \sum_i \frac{[C_\beta^i - C_\beta(\mathbf{q}_i, \mathbf{K}_i, \theta)]^2}{\sigma_i^2}, \quad (35)$$

where we explicitly show the dependence of  $\chi^2$  on the model parameters  $\theta$ . By varying these parameters to minimize  $\chi^2$ , we can find the best fit of the model to the data. Our programs can minimize  $\chi^2$  by using either the Simplex method or the Levenberg-Marquardt method [28].

## B. Confidence in the Overall Fit

By the central limit theorem, it is well known that the probability distribution of the sum of a very large number of small random deviations almost always converges to a normal distribution. In the remainder of this paper, we will assume that a sufficiently large number of measurements have been taken so that the measurement errors are normally distributed

around their true values. With this assumption as well as the assumption of a perfect model, the probability density  $\Pi_\nu$  of obtaining a minimum of  $\chi^2$  equal to  $\chi_{\min}^2$  is given by the chi-square function [28,29]

$$\Pi_\nu(\chi_{\min}^2) = \frac{1}{2\Gamma(\nu/2)} \exp(-\chi_{\min}^2/2) \left(\frac{\chi_{\min}^2}{2}\right)^{\nu/2-1}, \quad (36)$$

where  $\nu$  is the number of degrees of freedom of the fit. For a model with  $M$  adjustable parameters fit to  $N$  data points,  $\nu$  is simply  $N - M$ . Since the above distribution is single-peaked with a mean of  $\nu$  and a variance of  $\sqrt{2\nu}$ , it follows that for a perfect model the most probable values of  $\chi_{\min}^2$  per degree of freedom are close to one. A value of  $\chi_{\min}^2/\nu$  much larger than one corresponds to a small probability density and consequently leads one to question whether the model used is a good one or whether the error bars on the data have been underestimated. Conversely, a value of  $\chi_{\min}^2/\nu$  much less than one seems too good to be true and leads one to question whether the error bars on the data have been overestimated.

A more quantitative way to determine the “goodness” of the fit is to integrate  $\Pi_\nu(\chi^2)$  over  $\chi^2$  from the  $\chi_{\min}^2$  actually found in the fit to infinity. The resulting function  $\mathcal{P}_\nu(\chi_{\min}^2)$  is the probability that random measurement errors and a perfect model would lead to a minimum of  $\chi^2$  at least as big as the one actually found,  $\chi_{\min}^2$ . A fit to a “good” model results in a small  $\chi_{\min}^2$  and a  $\mathcal{P}_\nu(\chi_{\min}^2)$  which is greater than some acceptable probability (e.g., 5%). A fit to a “poor” model, on the other hand, results in a large  $\chi_{\min}^2$  and a small value of  $\mathcal{P}_\nu(\chi_{\min}^2)$ . If, for example, one obtained  $\mathcal{P}_\nu(\chi_{\min}^2) = 10^{-10}$ , it would be very difficult to believe that the large value of  $\chi_{\min}^2$  giving rise to that small probability had come about purely by way of random measurement errors; it is far more likely that there is something seriously wrong with the model. Of course, the choice of which probability should actually be used to draw the line between “good” and “bad” models is a purely subjective judgement. For our criterion, we choose that probability to be a few percent.

### C. Estimated Errors in the Parameters

Assuming the model is determined to be a “good” one, the parameters found at  $\chi_{\min}^2$  may reveal some interesting physics. If, for example, an unexpectedly low freezeout temperature is discovered in a fit, it is necessary to know how confident one can be in that particular low value. In other words, we need to estimate the possible error in that fitted parameter due to random measurement errors in the experiment. More generally, one would like to determine the region in  $M$ -dimensional parameter space which has a high probability of containing the underlying true parameter values. For example, we would like to be able to say “there is a 99% chance that the true parameter values fall within such and such region of parameter space.”

For normally distributed measurement errors, the relevant region is one consisting of all combinations of parameters  $\theta$  which would lead to a value of  $\chi^2(\theta)$  less than  $\chi_{\min}^2 + \Delta$ , where  $\Delta$  is some constant number. The confidence level “CL” for a specific  $\Delta$  and a specific number of parameters  $M$  is given by the integral of an  $M$ -degree-of-freedom chi-square distribution [28,29]:

$$\text{CL} = \int_0^\Delta d\chi^2 \Pi_M(\chi^2) \quad (37)$$

For example, if we choose a region defined by  $\Delta = 21.666$  for a model with  $M = 9$ , Eq. (37) tells us that  $\text{CL} = 0.99$ . This means that we have 99% confidence that the true parameter set lies among all possible sets which result in a  $\chi^2(\theta)$  less than  $\chi_{\min}^2 + 21.666$ . By inverting Eq. (37), it is possible to find the appropriate  $\Delta$  for  $M$  parameters which leads to any desired confidence level.

Once  $\Delta$  has been determined in this way, the desired region in parameter space is found by making a Taylor expansion of  $\chi^2(\theta)$  about its minimum at  $\bar{\theta}$ :

$$\chi^2(\theta) = \chi_{\min}^2 + \frac{1}{2} \sum_{a,b=1}^M (\theta_a - \bar{\theta}_a)(\theta_b - \bar{\theta}_b) \left. \frac{\partial^2 \chi^2}{\partial \theta_a \partial \theta_b} \right|_{\bar{\theta}} + \cdots \quad (38)$$

Notice that the gradient terms disappear because we are expanding around a minimum. If



we assume that higher-order terms are also negligible close to the minimum, then the desired region of parameter space is just the  $M$ -dimensional hyperellipsoidal volume defined by

$$\sum_{a,b=1}^M (\theta_a - \bar{\theta}_a) D_{ab} (\theta_b - \bar{\theta}_b) \leq \Delta, \quad (39)$$

where the curvature matrix  $D_{ab}$  is just one-half of the second derivative matrix of  $\chi^2$ .

From Eq. (35), it is apparent that the exact curvature matrix  $D_{ab}$  involves terms of the form

$$\left[ \frac{P_\alpha^i - P_\alpha(\mathbf{p}_i, \theta)}{\sigma_i^{\text{stat}2} + (f_\alpha P_\alpha^i)^2} \right] \frac{\partial^2 P_\alpha(\mathbf{p}_i, \theta)}{\partial \theta_a \partial \theta_b}$$

and

$$\left[ \frac{C_\beta^i - C_\beta(\mathbf{q}_i, \mathbf{K}_i, \theta)}{\sigma_i^2} \right] \frac{\partial^2 C_\beta(\mathbf{q}_i, \mathbf{K}_i, \theta)}{\partial \theta_a \partial \theta_b}.$$

For a good model,  $P_\alpha^i - P_\alpha$  and  $C_\beta^i - C_\beta$  are nothing more than the random measurement errors at the point  $i$ . Since these errors can have either sign and should in general be uncorrelated with the model, terms of the above form tend to cancel out when summed over  $i$ . By dropping these terms, we obtain the approximate curvature matrix that is actually used in the model:

$$\begin{aligned} D_{ab} = & \sum_{\alpha} \sum_i \frac{1}{\sigma_i^{\text{stat}2} + (f_\alpha P_\alpha^i)^2} \left( \frac{\partial P_\alpha(\mathbf{p}_i, \theta)}{\partial \theta_a} \right) \left( \frac{\partial P_\alpha(\mathbf{p}_i, \theta)}{\partial \theta_b} \right) \Big|_{\bar{\theta}} \\ & + \sum_{\beta} \sum_i \frac{1}{\sigma_i^2} \left( \frac{\partial C_\beta(\mathbf{q}_i, \mathbf{K}_i, \theta)}{\partial \theta_a} \right) \left( \frac{\partial C_\beta(\mathbf{q}_i, \mathbf{K}_i, \theta)}{\partial \theta_b} \right) \Big|_{\bar{\theta}}. \end{aligned} \quad (40)$$

The best and most complete way to specify the parameter confidence region is to calculate the above curvature matrix and then employ Eq. (39). However, in order to get a quick idea of the size of the region, it is useful to provide one-dimensional error estimates on each parameter. One way to do this is by determining the largest and smallest values of each parameter that can be obtained on the hyperellipsoid. For example, suppose we had only two parameters,  $T$  and  $v_t$ , and we determined that the confidence region was the interior of the ellipse shown in Fig. 3. The one-dimensional error estimates  $\delta T$  and  $\delta v_t$  shown in the figure would give one a rough idea of the size of the ellipse. One must be careful in using

these one-dimensional simplifications, however, since for example the point  $(T + \delta T, v_t + \delta v_t)$  lies outside the confidence region. Mathematical determination of the one-dimensional error estimates is derived in Appendix A for the adjusted parameters and in Appendix B for additional calculated quantities of physical interest.

## IV. FITTING TO E-802 DATA

### A. Description of the Data

Having developed our model, we used it to fit meson data from central Si + Au collisions at  $p_{\text{lab}}/A = 14.6 \text{ GeV}/c$  measured in experiment E-802 at the AGS [6–8]. As mentioned previously, we did not attempt to fit proton or deuteron data due to the difficulty of disentangling spectators from participants. The invariant one-particle multiplicity distributions for  $\pi^+$ ,  $\pi^-$ ,  $K^+$ , and  $K^-$  were obtained from an on-line database [7] and then organized into input files in which each line contained the information

$$y_{p,i} \quad p_{t,i} \quad P^i \quad \sigma_i^{\text{stat}}.$$

These data were presented in graphical form in [6], where it was estimated that systematic errors for all of the particles except  $K^-$ 's were 10–15%, while those for the  $K^-$ 's may have been as much as 20%. For our fits, we used constant systematic errors of 15% for pions and  $K^+$ 's and 20% for  $K^-$ 's.

In addition to these data, we obtained preliminary three-dimensional correlation data for both  $\pi^+$  and  $K^+$  [8]. For the correlation data, the momenta of the identical particles were measured relative to a fixed frame at  $y_{\text{lab}} = 1.25$ . Each two-particle event was then three-dimensionally binned according to the components  $q_z$ ,  $q_{\text{out}}$ , and  $q_{\text{side}}$  of its momentum difference. We use here the standard notation of  $z$  denoting the beam direction, “out” denoting the direction parallel to the component of the average momentum  $\mathbf{K}$  which is perpendicular to the beam, and “side” denoting the remaining transverse direction [30]. The convention was used that  $q_{\text{out}} = p_{1,\text{out}} - p_{2,\text{out}}$  is always positive [31]. Since this convention

identifies which particle is “particle 1” and which is “particle 2,” the remaining two momentum differences,  $q_z = p_{1,z} - p_{2,z}$  and  $q_{\text{side}} = p_{1,\text{side}} - p_{2,\text{side}}$ , can and did take either sign. In other words, there were bins with negative values of  $q_z$  and  $q_{\text{side}}$  as well as those with positive values. For each bin in  $\mathbf{q}$ , the average values of  $Y = \frac{1}{2}(y_1 + y_2)$  and  $K_t = \frac{1}{2}(p_{1,\text{out}} + p_{2,\text{out}})$  for the pairs in that bin were calculated and recorded. Thus, in the correlation input files, each line contained the information

$$\langle Y \rangle_i \quad \langle K_t \rangle_i \quad q_{z,i} \quad q_{\text{out},i} \quad q_{\text{side},i} \quad C^i \quad \sigma_i ,$$

where  $\langle \rangle_i$  represents the average value over the bin  $i$ .

Due to the very large number of correlation data points, not all of the data were used. In particular, for  $\pi^+$  we used only points for which the  $\mathbf{q}_i$  at the center of the bin satisfied the inequality

$$\left( \frac{q_z}{200} \right)^2 + \left( \frac{q_{\text{out}}}{100} \right)^2 + \left( \frac{q_{\text{side}}}{100} \right)^2 < 1 , \quad (41)$$

with the components of  $\mathbf{q}$  measured in MeV/ $c$ . Similarly, for  $K^+$  we used only data points satisfying

$$\left( \frac{q_z}{250} \right)^2 + \left( \frac{q_{\text{out}}}{125} \right)^2 + \left( \frac{q_{\text{side}}}{125} \right)^2 < 1 . \quad (42)$$

Our rationale for omitting some of the data points was that most of the physically important information is contained at low momentum differences. For momentum differences greater than those specified above, the model predicted a correlation function very close to one, while the actual data fluctuated wildly about this value with huge error bars. Furthermore, we found that the use of different momentum-difference cutoffs did not significantly affect our results.

Combining both the one-particle distributions and the two-particle correlations, we used a total of 1416 data points in our fits. Since there are nine adjustable parameters, there are 1407 degrees of freedom.

## B. Results of the Fit

The best-fit parameter values and their estimated errors (see Appendix A) at a 99% confidence level for the minimum  $\chi^2$  found are listed in Table I. Since the 99%-confidence hyperellipsoid overlaps an unphysical region in which  $\alpha_t < -1$ , the lower error estimate on  $\alpha_t$  has been reduced to reflect only the physical region. The curvature matrix  $D$  and its inverse, the covariance matrix  $D^{-1}$ , are presented in Tables II and III, respectively. Having found the minimum, it is possible to calculate a number of other related quantities of physical interest. Some of these are constrained parameters such as  $\mu_s$ , while others are calculated quantities such as the maximum longitudinal expansion velocity  $v_\ell = \tanh(\eta_0)$  achieved by the source in its center-of-mass frame. One of the most interesting of these quantities is the local baryon density at freezeout. Appendix B describes how each of the related quantities is calculated, while Table IV shows all of these quantities with their estimated errors.

The “goodness” of the fit can be seen by looking at Fig. 4, which shows a plot of the probability density  $\Pi_\nu$  of Eq. (36) for 1407 degrees of freedom versus  $\chi_{\min}^2$ . The high probability density of the resulting  $\chi_{\min}^2 = 1484.6$  is good evidence that there is nothing seriously wrong with the model. In fact, integration of the shaded region determines that there is a 7.4% chance of obtaining a value of  $\chi_{\min}^2$  at least that large when fitting an absolutely perfect model to the data. To get an idea of how much each data set contributed to the overall  $\chi_{\min}^2$ , we have broken down the individual contributions in Table V. Obviously, all of the data sets are fit reasonably well, although the  $\chi^2$  per degree of freedom for the negative-pion one-particle distribution is slightly higher than the rest.

The goodness of fit for the one-particle distributions can also be seen qualitatively by looking at direct comparisons of the model to the data. Figures 5–8 show the theoretical and experimental meson invariant one-particle multiplicity distributions as functions of  $m_t - m$  for various rapidities. As expected from the low value of  $\chi_{\min}^2$ , the overall agreement looks excellent.

Although proton data were not used for the main fit, once the best parameters have been

found, it is possible to calculate the proton distribution and compare it with the experimental data. Figure 9 shows that the model predictions agree with the proton data moderately well for rapidities of 1.3 or greater. For lower rapidities, however, the data show far more low- $p_t$  protons than are predicted by the model. In our picture, we consider these protons to be target spectators which may have interacted somewhat, but not enough to be considered part of the hydrodynamical system. It should also be noted that since our model does not distinguish between a deuteron and a separate proton and neutron, some of the excess when the model overpredicts the proton data may be due to leaving out deuteron coalescence.

As mentioned before, the main problem with including proton data in the fits is figuring out how to eliminate contamination by spectators. Nevertheless, in order to get some idea of how the inclusion of protons might affect our results, we made four different fits in which we included all proton data in the following rapidity ranges:  $1.5 \leq y_p \leq 1.9$ ,  $1.3 \leq y_p \leq 1.9$ ,  $1.5 \leq y_p \leq 2.1$ , and  $1.3 \leq y_p \leq 2.1$ . These fits all give extremely similar results, so we will discuss only the last case. The 190 proton data points for this case bring the number of degrees of freedom up to 1597. The minimum  $\chi^2$  of 1730.4 ( $\chi^2/\nu = 1.084$ ) is obtained with the following parameters:  $T = 95.8 \pm 3.9$  MeV,  $\mu_b/T = 5.30 \pm 0.28$ ,  $\lambda_\pi = 0.66 \pm 0.11$ ,  $R = 7.8 \pm 1.5$  fm,  $v_t = 0.640 \pm 0.034$   $c$ ,  $\alpha_t = -0.87^{+0.35}_{-0.13}$ ,  $y_s = 1.320 \pm 0.072$ ,  $\eta_0 = 1.48 \pm 0.14$ , and  $\tau_f = 8.1 \pm 2.1$  fm/ $c$ . The central values themselves for all of the parameters except  $\mu_b/T$  lie within the individual 99%-confidence intervals of the original fit (see Table I). Even for  $\mu_b/T$ , the 99%-confidence interval for the fit with protons overlaps that for the original fit. In other words, inclusion of the proton data changes the best-fit parameter values only within their stated uncertainties. It does, however, lead to a significant reduction in the calculated number of projectile participants. For the fit with protons included, the number of projectile participants is reduced to  $17.7 \pm 1.4$ , which is to be compared to  $26.1^{+8.8}_{-6.7}$  found in Table IV and to 28 nucleons in a  $^{28}\text{Si}$  nucleus. If one were to take the proton fit seriously, one might wonder how a central Si + Au collision could possibly give rise to 10 projectile spectators. It is our view that the unresolved issues of coalescence and spectator separation in our model make it better to simply neglect the protons altogether, just as we did in our

original fit. For the remainder of the paper, we will always refer only to that original fit.

Since the preliminary correlation data that was used has not yet been published, we show here in Figs. 10 and 11 ( $q_z, q_{\text{out}}$ ) projections of the correlation functions calculated by the model. Notice that whereas the kaon correlation function intercepts the  $\mathbf{q} = 0$  axis at 2, the pion correlation function intercepts the axis at 1.65, corresponding to a value of  $\lambda_\pi = 0.65$ . Notice also that since nonvanishing values of both  $K_t$  and  $Y - y_s$  are used for the plots, the effects of the “out-long” cross term [22,32,33] can be seen (especially in the kaons) as a slight twisting in the major axes of the correlation function.

Data from central Si + Au collisions at the AGS have also been compared to a thermal model in [34]. There it was argued that a freezeout temperature of 120–140 MeV was consistent with these data. We, on the other hand, have found a much lower temperature of  $92.9 \pm 4.4$  MeV (see Table I). To explain this significant discrepancy, we would like to point out a few differences between our approach and that of [34]. First of all, they assumed that transverse and longitudinal flow are completely separable. This led them to compare a thermal model that had been integrated over all rapidities [21] with data from a single mid-rapidity bin. In contrast, we make no such assumption. Secondly, the model used in [34] never specifies the size or shape of the freezeout hypersurface. In addition to preventing comparisons to two-particle correlations, this ambiguity forces them to multiply each of their one-particle distributions by an arbitrary normalization factor before comparing to the normalized data of [6]. Not only does our unambiguous parametrization of the freezeout hypersurface allow us to compare to two-particle correlations, it also allows us to see the significant effects that different temperatures have on the absolute normalizations of one-particle distributions. Another significant difference between the two approaches is that in [34] only two points in temperature were studied, whereas in our approach the whole nine-dimensional parameter space is explored, resulting in the absolute minimum of  $\chi^2$ .

In order to see how much worse higher temperature fits would be, we made a number of runs at various fixed temperatures, allowing all of the other parameters to vary. The results are given in Table VI and in Fig. 12, a plot of the minimum  $\chi^2$  at a fixed temperature vs.

that temperature. As Table VI shows, the value of  $\chi^2$  for  $T = 120$  MeV is 2025.4. Again by integrating  $\Pi_\nu$  of Eq. (36), we can determine that the probability of a perfect model resulting in a  $\chi^2$  at least as large as 2025.4 is the incredibly small value  $5.1 \times 10^{-25}$ . Above  $T = 129$  MeV, the minimum  $\chi^2$  solution switches to a different branch. This high-temperature branch is actually unphysical, as can be seen by examining Table VI and noting that it is impossible for the system to expand to the large transverse radius  $R$  in the infinitesimally small time  $t_1 = \tau_f \sqrt{1 + \alpha_t}$ .

Another result of the model is the size and shape of the freezeout hypersurface. Since  $\alpha_t$  for the best fit is negative, freezeout begins at time  $t = t_1 = 3.1$  fm/ $c$  at  $z = 0$  and  $\rho = R = 8.0$  fm, and takes 5.1 fm/ $c$  to reach the center of the source at  $z = \rho = 0$  at time  $t = t_2 = \tau_f = 8.2$  fm/ $c$ . Freezeout along the symmetry axis then occurs at a constant proper time, finally ending at source-frame time  $t_3 = \tau_f \cosh \eta_0 = 18.8$  fm/ $c$ . As mentioned previously, Figs. 1 and 2 pictorially show the freezeout process for these parameter values.

## V. FUTURE ISSUES

The actual “freezeout” process taking place in these collisions is undoubtedly far more complicated than in our model. Azimuthal symmetry may be broken, the local temperature and chemical potentials may have some spacetime dependence, the expansion flow velocity may be neither boost-invariant nor linear in  $\rho$ , the hypersurface may have a different shape and/or some four-dimensional fuzziness, kaons may freeze out before pions, chemical equilibrium may not be fully achieved, etc. One may even question whether equilibrium hydrodynamical concepts are valid at all. Although this paper does not definitively settle these questions, the remarkable agreement between theory and experiment suggests that our realistic nine-parameter expanding source model nevertheless provides a very good description of the most important physics taking place at freezeout.

One parameter which definitely needs to be better understood is the incoherence parameter  $\lambda_\pi$ . Does the fact that it is less than one mean that a significant number of pions

are being produced coherently, or could the reduced intercept instead be largely an artifact arising from the way the correlation function was determined experimentally [35]?

We hope that our model will be used in the future to systematically analyze the dependence of the freezeout quantities upon bombarding energy and the sizes of the colliding nuclei. A sharp discontinuity in one or more of these quantities could be a signal of quark-gluon-plasma formation.

## ACKNOWLEDGMENTS

We are grateful to Arnold J. Sierk for his participation in the early stages of this work, to Bernd R. Schlei for illuminating discussions about hydrodynamics and freezeout hypersurfaces, and to T. Vincent A. Cianciolo for permitting us to use his preliminary data on two-particle correlations in our adjustments. This work was supported by the U. S. Department of Energy.

## APPENDIX A: ONE-DIMENSIONAL ERROR PROJECTIONS

The simplest way to determine the largest and smallest values attained by parameter  $\theta_a$  on the hyperellipsoid defined by Eq. (39) is to use a Lagrange multiplier  $\xi_a$ . We begin by finding the maximum (or minimum) of the quantity

$$\theta_a - \xi_a \sum_{b,c=1}^M (\theta_b - \bar{\theta}_b) D_{bc} (\theta_c - \bar{\theta}_c) .$$

By differentiating with respect to  $\theta_d$ , we find the coordinates  $\theta_e$  of the extrema as a function of  $\xi_a$ :

$$\theta_e - \bar{\theta}_e = \frac{1}{2\xi_a} \left( D^{-1} \right)_{ea} , \tag{A1}$$

where the subscripts  $a$  are not summed over. To impose the constraint that the solution lies on the hyperellipsoid, we must pick a  $\xi_a$  such that the equality of Eq. (39) is satisfied. Plugging Eq. (A1) into Eq. (39) and solving for  $\xi_a$ , we find



$$2\xi_a = \pm \sqrt{\frac{(D^{-1})_{aa}}{\Delta}}, \quad (\text{A2})$$

where again the indices  $a$  are not summed over. Inserting Eq. (A2) into Eq. (A1), we find the values of all of the parameters  $\theta_e$  corresponding to each extremum of  $\theta_a$  on the hyperellipsoid. In particular, the one-dimensional error estimate on  $\theta_a$  is just proportional to the square root of the  $aa$ th element of the covariance matrix (the inverse of the curvature matrix):

$$\theta_a - \bar{\theta}_a = \pm \sqrt{\Delta (D^{-1})_{aa}}. \quad (\text{A3})$$

By inverting the curvature matrix to get the covariance matrix, one can then just read off the one-dimensional error estimate on each parameter by taking the square root of the product of the appropriate diagonal element times  $\Delta$ .

## APPENDIX B: ADDITIONAL CALCULATED QUANTITIES

Here we list some additional physical quantities of interest which can be calculated from the nine parameters. From Eqs. (7) and (18), it can be seen that the maximum longitudinal velocity achieved by the source is given by  $v_\ell = \tanh \eta_0$ . Also, in Sec. II.B the times that freezeout begins, reaches the center of the source, and ends were shown to be  $t_1 = \tau_f \sqrt{1 + \alpha_t}$ ,  $t_2 = \tau_f$ , and  $t_3 = \tau_f \cosh \eta_0$ , respectively. The maximum longitudinal extension of the source is given by  $z_3 = \tau_f \sinh \eta_0$ , while the duration of freezeout at  $z = 0$  is given by  $\Delta t = t_2 - t_1$ . The total baryon number  $B_{\text{tot}}$  of the source is given by the denominator of the second equation in (21). Section II.C also explains how the chemical potentials  $\mu_s$  and  $\mu_i$  are found. The numbers of projectile and target participants can be deduced from Eq. (23) and are given by

$$\begin{aligned} B_{\text{proj}} &= \frac{B_{\text{tot}} \sinh(y_s - y_{\text{tar}})}{\sinh(y_s - y_{\text{tar}}) + \sinh(y_{\text{proj}} - y_s)} \\ B_{\text{tar}} &= \frac{B_{\text{tot}} \sinh(y_{\text{proj}} - y_s)}{\sinh(y_{\text{proj}} - y_s) + \sinh(y_s - y_{\text{tar}})}. \end{aligned} \quad (\text{B1})$$

The local density of particles of type  $\alpha$  is given by the integral

$$\begin{aligned}
n_\alpha(\rho) &= \frac{1}{\gamma_\rho \cosh \eta} \int \frac{d^3 p}{E} \int dt S(x, p) . \\
&= \frac{J_\alpha(J_\alpha + 1)}{2\pi^2 \gamma_\rho} \sum_{k=1}^{\infty} (-1)^k \exp(k\mu_\alpha/T) \int m_t dm_t \left[ m_t K_1 \left( \frac{k\gamma_\rho m_t}{T} \right) I_0 \left( \frac{K\gamma_\rho p_t v_t \rho}{RT} \right) \right. \\
&\quad \left. - \frac{\alpha_t p_t \rho \tau_f}{R^2 \sqrt{1 + \alpha_t(\rho/R)^2}} K_0 \left( \frac{k\gamma_\rho m_t}{T} \right) I_1 \left( \frac{K\gamma_\rho p_t v_t \rho}{RT} \right) \right] , \tag{B2}
\end{aligned}$$

where  $K_i$  and  $I_i$  are modified Bessel functions of order  $i$ . Due to the boost invariance assumed in everything but the spatial limits of the model,  $n_\alpha$  is a function of only  $\rho$  and not of  $\eta$ . The local baryon density is just given by

$$n_b(\rho) = \sum_{\alpha} B_\alpha n_\alpha(\rho) . \tag{B3}$$

To calculate error estimates on these quantities, we could in principle use a more general form of the Lagrange-multiplier method introduced in Appendix A. We have found, however, that a quicker and more reliable method is to first find  $M - 1$  new variables which can parametrize just the surface of the hyperellipsoid, express the quantities as functions of these new variables, and then find the extrema of these functions. We begin this process by numerically finding the unitary matrix  $U$  which transforms  $D$  into the diagonal matrix  $\tilde{D}$ , namely

$$\tilde{D} = U^{-1} D U . \tag{B4}$$

Next we use the (diagonal) elements of  $\tilde{D}$  to define the vector

$$\psi_a = \sqrt{\frac{\tilde{D}_{aa}}{\Delta}} \sum_{b=1}^M (U^{-1})_{ab} (\theta_b - \bar{\theta}_b) , \tag{B5}$$

where there is no summation over the index  $a$ . Using these variables, we can see that the equality of Eq. (39) reduces to the equation of the surface of a sphere in  $M$  dimensions, namely

$$\sum_{a=1}^M \psi_a^2 = 1 . \tag{B6}$$

Since the surface is  $(M - 1)$ -dimensional,  $M - 1$  angles are sufficient to identify any point on it. We now redefine the  $\psi_a$  in terms of the angles  $\phi_a$  through

$$\begin{aligned}
\psi_1 &= \cos(\phi_1) \\
\psi_2 &= \sin(\phi_1) \cos(\phi_2) \\
&\vdots \\
\psi_{M-1} &= \sin(\phi_1) \sin(\phi_2) \cdots \sin(\phi_{M-2}) \cos(\phi_{M-1}) \\
\psi_M &= \sin(\phi_1) \sin(\phi_2) \cdots \sin(\phi_{M-2}) \sin(\phi_{M-1}) .
\end{aligned} \tag{B7}$$

Since the inverse of Eq. (B5) tells us

$$\theta_a = \bar{\theta}_a + \sqrt{\frac{\Delta}{\tilde{D}_{aa}}} \sum_{b=1}^M U_{ab} \psi_b , \tag{B8}$$

we now have the  $M$  parameters  $\theta_a$  expressed in terms of the  $M - 1$  parameters  $\phi_a$ . As mentioned previously, the extrema on the hyperellipsoid for any function  $f(\theta(\phi))$  can be found simply by allowing the  $\phi_a$  to vary freely.

## REFERENCES

- [1] H. Satz, *Ann. Rev. Nucl. Part. Sci.* **35**, 245 (1985).
- [2] E. V. Shuryak, *The QCD Vacuum, Hadrons and the Superdense Matter*, Part 3 (World Scientific, Singapore, 1988).
- [3] C.-Y. Wong, *Introduction to High-Energy Heavy-Ion Collisions* (World Scientific, Singapore, 1994).
- [4] *Quark Matter '95, Proc. Eleventh Int. Conf. on Ultra-Relativistic Nucleus-Nucleus Collisions, Monterey, California, 1995*, *Nucl. Phys.* **A590**, 1c (1995).
- [5] B. R. Schlei, U. Ornik, M. Plümer, D. Strottman, and R. M. Weiner, Los Alamos Preprint No. LA-UR-95-3232, Los Alamos e-print archive, <http://xxx.lanl.gov/hep-ph/9509426> (1995), and references therein.
- [6] T. Abbott *et al.*, E-802 Collaboration, *Phys. Rev.* **C50**, 1024 (1994).
- [7] National Nuclear Data Center, <http://necs01.dne.bnl.gov/html/nndc.html>, NNDC On-line Data Service, Data Base CSISRS, Accession Number C0501.
- [8] T. V. A. Cianciolo (E-802 Collaboration), private communication.
- [9] B. R. Schlei, U. Ornik, M. Plümer, and R. M. Weiner, *Phys. Lett.* **B293**, 275 (1992); J. Bolz, U. Ornik, M. Plümer, B. R. Schlei, and R. M. Weiner, *Phys. Lett.* **B300**, 404 (1993).
- [10] F. Cooper and G. Frye, *Phys. Rev.* **D10**, 186 (1974).
- [11] E. Shuryak, *Phys. Lett.* **B44**, 387 (1973); *Sov. J. Nucl. Phys.* **18**, 667 (1974).
- [12] S. Pratt, T. Csörgő, and J. Zimányi, *Phys. Rev.* **C42**, 2646 (1990).
- [13] I. V. Andreev, M. Plümer, and R. M. Weiner, *Int. J. Mod. Phys.* **A8**, 4577 (1993).
- [14] S. Chapman and U. Heinz, *Phys. Lett.* **B340**, 250 (1994).

- [15] G. F. Bertsch, P. Danielewicz, and M. Herrmann, Phys. Rev. **C49**, 442 (1994).
- [16] F. Cooper, G. Frye, and E. Schonberg, Phys. Rev. **D11**, 192 (1975).
- [17] J. D. Bjorken, Phys. Rev. **D27**, 140 (1983).
- [18] S. Esumi, S. Chapman, H. van Hecke, and Nu Xu, in preparation.
- [19] U. Ornik, M. Plümer, B. R. Schlei, D. Strottman, and R. M. Weiner, in preparation.
- [20] U. Mayer, E. Schnedermann, and U. Heinz, Phys. Lett. **B294**, 69 (1992).
- [21] E. Schnedermann, J. Sollfrank, and U. Heinz, in *Particle Production in Highly Excited Matter*, edited by E. H. Gutbrod and J. Rafelski (Plenum Press, New York, 1992), p. 175.
- [22] S. Chapman, P. Scotto, and U. Heinz, Phys. Rev. Lett. **74**, 4400 (1995).
- [23] T. Csörgő and B. Lørstad, Nucl. Phys. **A590**, 465 (1995).
- [24] J. Sollfrank, P. Koch, and U. Heinz, Phys. Lett. **B252**, 256 (1990).
- [25] J. Bolz, U. Ornik, M. Plümer, B. R. Schlei, and R. M. Weiner, Phys. Rev. **D47**, 3860 (1993).
- [26] R. Hagedorn, *Relativistic Kinematics* (W. A. Benjamin, New York, 1963).
- [27] L. Montanet *et al.*, Particle Data Group, Phys. Rev. **D50**, 1173 (1994).
- [28] W. H. Press, S. A. Teukolsky, W. T. Vetterling, and B. P. Flannery, *Numerical Recipes in Fortran: The Art of Scientific Computing*, Second Edition (Cambridge University Press, Cambridge, 1992), Secs. 10.4 and 15.4–15.6.
- [29] A. G. Frodesen, O. Skjeggstad, and H. Tøfte, *Probability and Statistics in Particle Physics* (Universitetsforlaget, Oslo, 1979), pp. 128, 288, and 316.
- [30] G. Bertsch, M. Gong, and M. Tohyama, Phys. Rev. **C37**, 1896 (1988).

- [31] S. Chapman, J. R. Nix, and U. Heinz, Phys. Rev. **C52**, 2694 (1995).
- [32] S. Chapman, P. Scotto, and U. Heinz, Los Alamos e-print archive, <http://xxx.lanl.gov>, hep-ph/9409349, Heavy Ion Physics **1**, 1 (1995).
- [33] S. Chapman, P. Scotto, and U. Heinz, in *Quark Matter '95, Proc. Eleventh Int. Conf. on Ultra-Relativistic Nucleus-Nucleus Collisions, Monterey, California, 1995*, Nucl. Phys. **A590**, 449c (1995).
- [34] P. Braun-Munzinger, J. Stachel, J. P. Wessels, and N. Xu, Phys. Lett. **B344**, 43 (1995).
- [35] In private communication, B. V. Jacak informed us that in her experience with NA44 correlation data, it is possible to obtain very different values for  $\lambda_\pi$ , depending on the experimental acceptance.

## FIGURES

FIG. 1. Freezeout hypersurface, which specifies the positions in spacetime where the expanding hydrodynamical fluid is converted into a collection of noninteracting, free-streaming hadrons. The parameters used are  $R = 8.0$  fm,  $\tau_f = 8.2$  fm/ $c$ ,  $\eta_0 = 1.47$ , and  $\alpha_t = -0.86$ .

FIG. 2. Seven snapshots at equal spacings in the source-frame time  $t$  of the part of the source of Fig. 1 that is freezing out (inner surfaces) or has not yet frozen out (end caps). To draw the end caps at each time  $t$ , we used  $v_t = 0.683$   $c$  and assumed that none of the fluid was accelerated prior to reaching the freezeout hypersurface.

FIG. 3. An example 99%-confidence ellipse for a model with two parameters showing how one-dimensional errors on those parameters are estimated.

FIG. 4. The probability density  $\Pi_\nu$  of Eq. (36) for obtaining a particular minimum of  $\chi^2$  from a fit with 1407 degrees of freedom  $\nu$  to a perfect model. There is a 7.4% chance that a perfect model would have given rise to a  $\chi_{\min}^2$  at least as large as the one actually found, 1484.6.

FIG. 5. Comparison between model predictions and experimental data [6,7] for the invariant  $\pi^+$  one-particle multiplicity distribution  $Ed^3N/dp^3 = 1/(2\pi m_t) d^2N/dy_p dm_t$  as a function of  $y_p$  and  $m_t - m$ . For visual separation, the results at a particular particle rapidity  $y_p$  relative to the laboratory frame are scaled by the factor  $10^{5(0.7-y_p)}$ . Although not always distinguishable on the scale of the graphs, statistical errors are given by the inner error bars, and total errors are given by the outer error bars in Figs. 5–9.

FIG. 6. Comparison between model and experimental  $\pi^-$  distributions, scaled as in Fig. 5.

FIG. 7. Comparison between model and experimental  $K^+$  distributions, scaled as in Fig. 5.

FIG. 8. Comparison between model and experimental  $K^-$  distributions, scaled as in Fig. 5.

FIG. 9. Comparison between model and experimental proton distributions, scaled as in Fig. 5. Note that these proton data were not included in the fit.

FIG. 10. Dependence of the predicted  $\pi^+$  two-particle correlation function  $C$  upon the longitudinal and “out” momentum differences, for fixed values of the other three quantities upon which  $C$  depends.

FIG. 11. Dependence of the predicted  $K^+$  two-particle correlation function  $C$  upon the longitudinal and “out” momentum differences, for fixed values of the other three quantities upon which  $C$  depends.

FIG. 12. Minima of  $\chi^2$  for fixed values of  $T$ , when all other parameters are allowed to vary. Solid circles connected by a solid line identify one branch which contains some physically relevant solutions near the minimum, while open circles connected by a dashed line represent a different branch containing only unphysical solutions (see Table VI).



# TABLES

TABLE I. Nine adjusted source freezeout parameters.

Parameter	Value and uncertainty at 99% confidence
Nuclear temperature $T$	$92.9 \pm 4.4$ MeV
Baryon chemical potential $\mu_b/T$	$5.97 \pm 0.56$
Pion incoherence fraction $\lambda_\pi$	$0.65 \pm 0.11$
Transverse freezeout radius $R$	$8.0 \pm 1.6$ fm
Transverse freezeout velocity $v_t$	$0.683 \pm 0.048$ $c$
Transverse freezeout coefficient $\alpha_t$ <sup>a</sup>	$-0.86^{+0.37}_{-0.14}$
Source rapidity $y_s$	$1.355 \pm 0.066$
Longitudinal spacetime rapidity $\eta_0$	$1.47 \pm 0.13$
Longitudinal freezeout proper time $\tau_f$	$8.2 \pm 2.2$ fm/ $c$

<sup>a</sup>Physically,  $\alpha_t$  cannot be less than  $-1$ , since that value corresponds to freezeout beginning immediately at  $t = 0$ .

TABLE II. Curvature matrix  $D$ . Derivatives with respect to the parameters are ordered in rows and columns in the same way as for the parameters in Table I. The units of each element are given by the inverse of the units of the associated row and column parameters (e.g., the units of  $D_{14}$  are  $1/(\text{MeV}\cdot\text{fm})$ ).

	65.72	117.4	-11.16	175.6	1859	-54.69	606.7	524.4	140.5
	117.4	393.1	-9.373	295.8	1717	-36.53	867.3	740.1	222.9
	-11.16	-9.373	2017	-127.6	368.7	100.0	-110.7	-124.2	-82.88
	175.6	295.8	-127.6	509.4	4641	-169.9	1761	1501	395.3
$D =$	1859	1717	368.7	4641	87117	-2530	13964	14133	4107
	-54.69	-36.53	100.0	-169.9	-2530	313.5	-678.5	-580.9	-123.0
	606.7	867.3	-110.7	1761	13964	-678.5	19418	10296	1315
	524.4	740.1	-124.2	1501	14133	-580.9	10296	7643	1158
	140.5	222.9	-82.88	395.3	4107	-123.0	1315	1158	319.0

TABLE III. Covariance matrix  $D^{-1}$ . The ordering of the rows and columns is the same as in Table II. The units of each element are  $10^4$  times the inverse of the units in Table II (e.g., the units of  $(D^{-1})_{14}/10^4$  are  $\text{MeV}\cdot\text{fm}$ ).

	8860	-891.5	-53.42	-1180	-61.21	-121.3	-11.63	-29.23	-935.8
	-891.5	143.9	2.678	76.55	7.407	5.523	1.195	4.962	81.77
	-53.42	2.678	5.827	6.837	-0.04256	-1.918	0.04292	-0.3064	15.44
	-1180	76.55	6.837	1244	24.25	146.0	1.241	-8.943	-1302
$D^{-1} =$	-61.21	7.407	-0.04256	24.25	1.080	4.091	0.1796	0.04903	-21.53
	-121.3	5.523	-1.918	146.0	4.091	61.51	0.1794	0.9064	-164.8
	-11.63	1.195	0.04292	1.241	0.1796	0.1794	1.998	-3.112	3.576
	-29.23	4.962	-0.3064	-8.943	0.04903	0.9064	-3.112	8.359	2.626
	-935.8	81.77	15.44	-1302	-21.53	-164.8	3.576	2.626	2193

TABLE IV. Additional calculated physical quantities.

Quantity	Value and uncertainty at 99% confidence
Source velocity $v_s$	$0.875^{+0.015}_{-0.016} c$
Longitudinal velocity $v_\ell$	$0.900^{+0.023}_{-0.029} c$
Longitudinal freezeout radius $z_3$	$16.9^{+5.6}_{-4.9} \text{ fm}$
Beginning freezeout time $t_1$	$3.1^{+2.5}_{-3.1} \text{ fm}/c$
Freezeout time $t_2$ at source center	$8.2 \pm 2.2 \text{ fm}/c$
Final freezeout time $t_3$	$18.8^{+5.8}_{-5.3} \text{ fm}/c$
Freezeout width $\Delta\tau$ in proper time <sup>a</sup>	$5.9^{+4.4}_{-2.6} \text{ fm}/c$
Baryon chemical potential $\mu_b$	$554^{+34}_{-36} \text{ MeV}$
Strangeness chemical potential $\mu_s$	$75^{+13}_{-12} \text{ MeV}$
Isospin chemical potential $\mu_i$	$-5.3^{+1.0}_{-1.1} \text{ MeV}$
Number $B_{\text{proj}}$ of baryons originating from projectile	$26.1^{+8.8}_{-6.7}$
Number $B_{\text{tar}}$ of baryons originating from target	$57^{+20}_{-15}$
Total number $B_{\text{tot}}$ of baryons in source	$83^{+28}_{-21}$
Baryon density $n_1$ at beginning of freezeout <sup>b</sup>	$0.057^{+\infty}_{-0.032} \text{ fm}^{-3}$
Baryon density $n_s$ along symmetry axis	$0.0222^{+0.0096}_{-0.0069} \text{ fm}^{-3}$

<sup>a</sup>Calculated under the additional assumption that the exterior matter at  $z = 0$  that freezes out first has been moving with constant transverse velocity  $v_t$  from time  $t = 0$  until time  $t_1$ .

<sup>b</sup>The upper limit of  $\infty$  for this quantity arises because the beginning freezeout time  $t_1$  could be zero, at which time the shape is an infinitesimally thin disk.

TABLE V. Individual contributions to  $\chi^2$ .

Type of data	$N_{\text{data}}$	$\nu^{\text{a}}$	$\chi^2$	$\chi^2/\nu$
$\pi^+$ one-particle	231	229.5	238.0	1.037
$\pi^-$ one-particle	239	237.5	266.2	1.121
$K^+$ one-particle	137	136.1	140.6	1.033
$K^-$ one-particle	49	48.7	51.2	1.051
$\pi^+$ correlation	464	461.1	498.0	1.080
$K^+$ correlation	296	294.1	290.7	0.988
Total	1416	1407.0	1484.6	1.055

<sup>a</sup>In determining the number of degrees of freedom for the individual contributions, we have allocated the nine adjustable parameters among each type of data in proportion to the number of data points.

TABLE VI. Eight adjusted parameters of best fits at fixed values of temperature  $T$  plus calculated  $B_{\text{proj}}$ . Physically relevant solutions correspond only to a limited region surrounding the absolute minimum at  $T = 92.9$  MeV. For values of  $T$  below 82 MeV, the calculated lower limit on  $B_{\text{proj}}$  exceeds the number of nucleons in the projectile. Solutions below the horizontal line correspond to a new branch which is unphysical for the reason mentioned in the text.

$\chi^2$	$T$ (MeV)	$\mu_b/T$	$\lambda_\pi$	$R$ (fm)	$v_t$ (c)	$\alpha_t$	$y_s$	$\eta_0$	$\tau_f$ (fm/c)	$B_{\text{proj}}$
3280.7	50	16.4	1.02	21.1	0.971	0.232	1.467	1.75	10.2	566
2557.2	60	12.7	0.868	14.2	0.920	-0.523	1.428	1.70	10.8	204
2043.2	70	9.98	0.777	11.1	0.854	-0.671	1.394	1.64	10.5	88.9
1678.9	80	7.76	0.723	9.64	0.778	-0.738	1.375	1.55	9.65	41.9
1494.6	90	6.28	0.667	8.39	0.705	-0.818	1.361	1.49	8.47	27.8
1534.4	100	5.35	0.613	7.07	0.631	-0.999	1.341	1.46	7.55	23.6
1739.1	110	4.68	0.544	6.13	0.568	-0.999	1.315	1.47	6.44	21.6
2025.4	120	4.17	0.486	5.24	0.502	-0.999	1.284	1.49	5.69	20.1
2323.9	130	3.81	0.473	3.42	0.383	-0.999	1.266	1.54	7.40	19.2
2437.8	135	3.70	0.545	2.37	0.281	-0.999	1.268	1.57	10.3	19.3
2304.5	125	7.17	0.530	13.5	0.872	-0.999	1.380	1.47	0.133	72.5
2294.2	130	7.05	0.530	13.3	0.866	-0.999	1.379	1.47	0.102	68.2
2273.1	140	6.85	0.529	13.0	0.854	-0.999	1.375	1.45	0.0630	60.3
2252.2	150	6.69	0.528	12.7	0.839	-0.999	1.371	1.43	0.0407	53.2
2230.9	160	6.60	0.528	12.4	0.823	-0.999	1.268	1.41	0.0269	45.8
2209.3	170	6.54	0.530	12.1	0.804	-0.999	1.365	1.39	0.0183	37.5
2190.9	180	6.41	0.532	11.9	0.783	-0.999	1.364	1.36	0.0139	31.1
2182.1	190	6.20	0.533	11.6	0.760	-0.999	1.361	1.35	0.0116	28.4
2185.2	200	5.96	0.536	11.4	0.738	-0.999	1.359	1.33	0.0103	27.7
2199.9	210	5.76	0.537	11.1	0.713	-0.999	1.353	1.32	0.00905	26.4
2228.1	220	5.57	0.537	10.9	0.690	-0.999	1.347	1.32	0.00805	27.0
2271.9	230	5.28	0.542	10.7	0.666	-0.999	1.333	1.33	0.00765	26.7
2335.3	240	4.99	0.544	10.5	0.637	-0.999	1.325	1.34	0.00756	28.1
2407.0	250	4.73	0.545	10.2	0.605	-0.999	1.319	1.34	0.00748	28.7

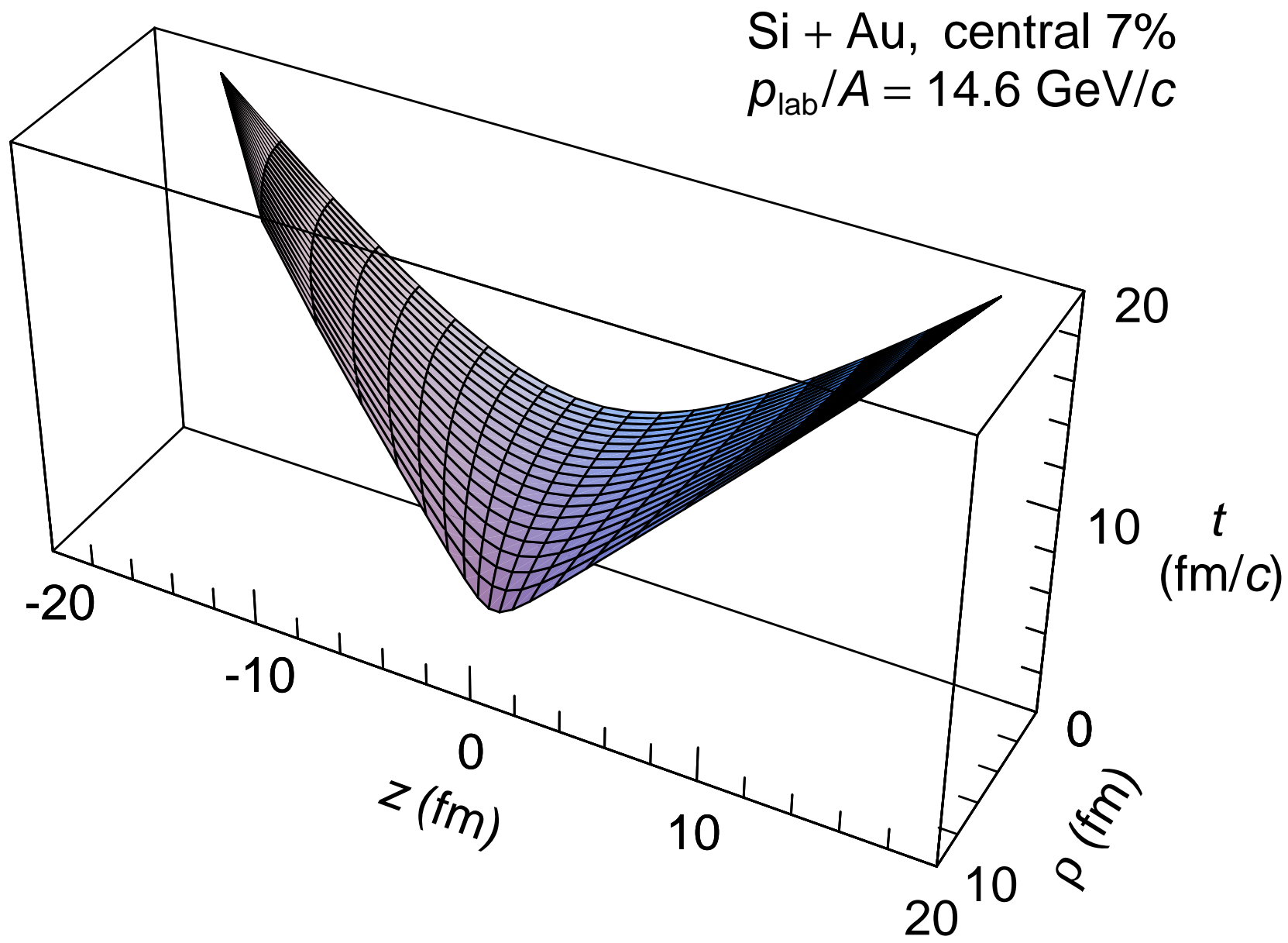


Figure 1

Source freezeout  
Si + Au, central 7%  
 $p_{\text{lab}}/A = 14.6 \text{ GeV}/c$

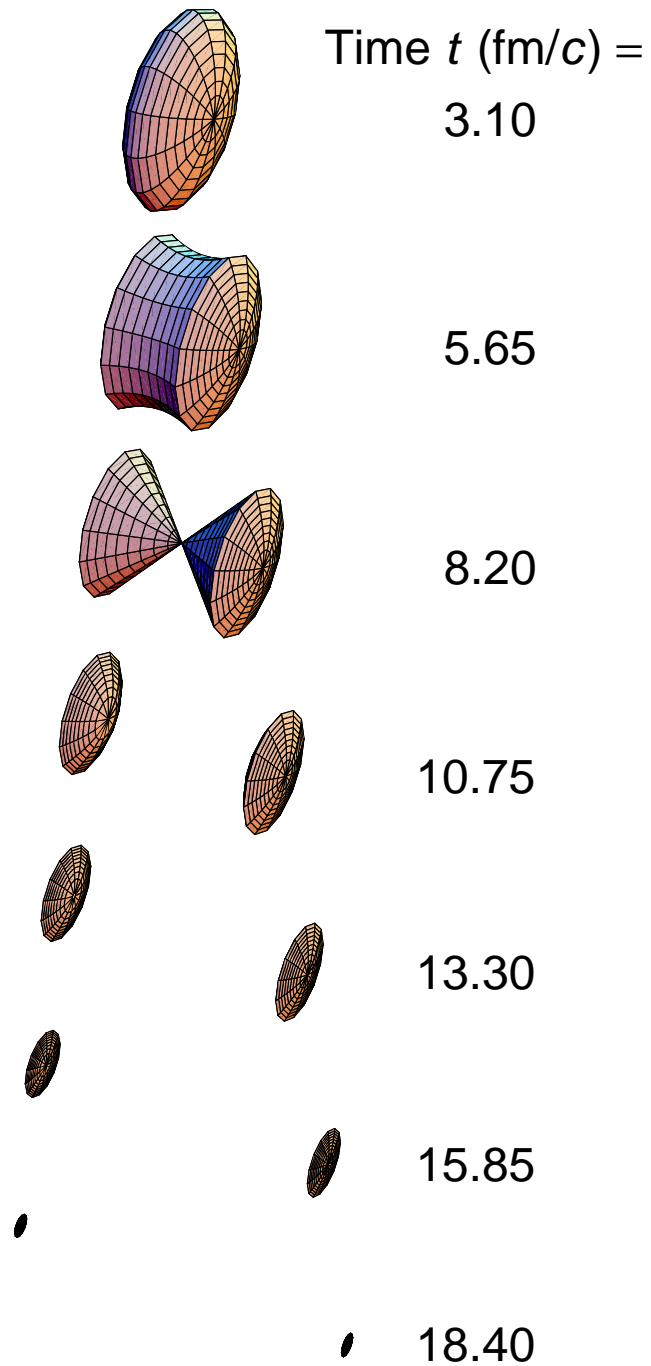


Figure 2

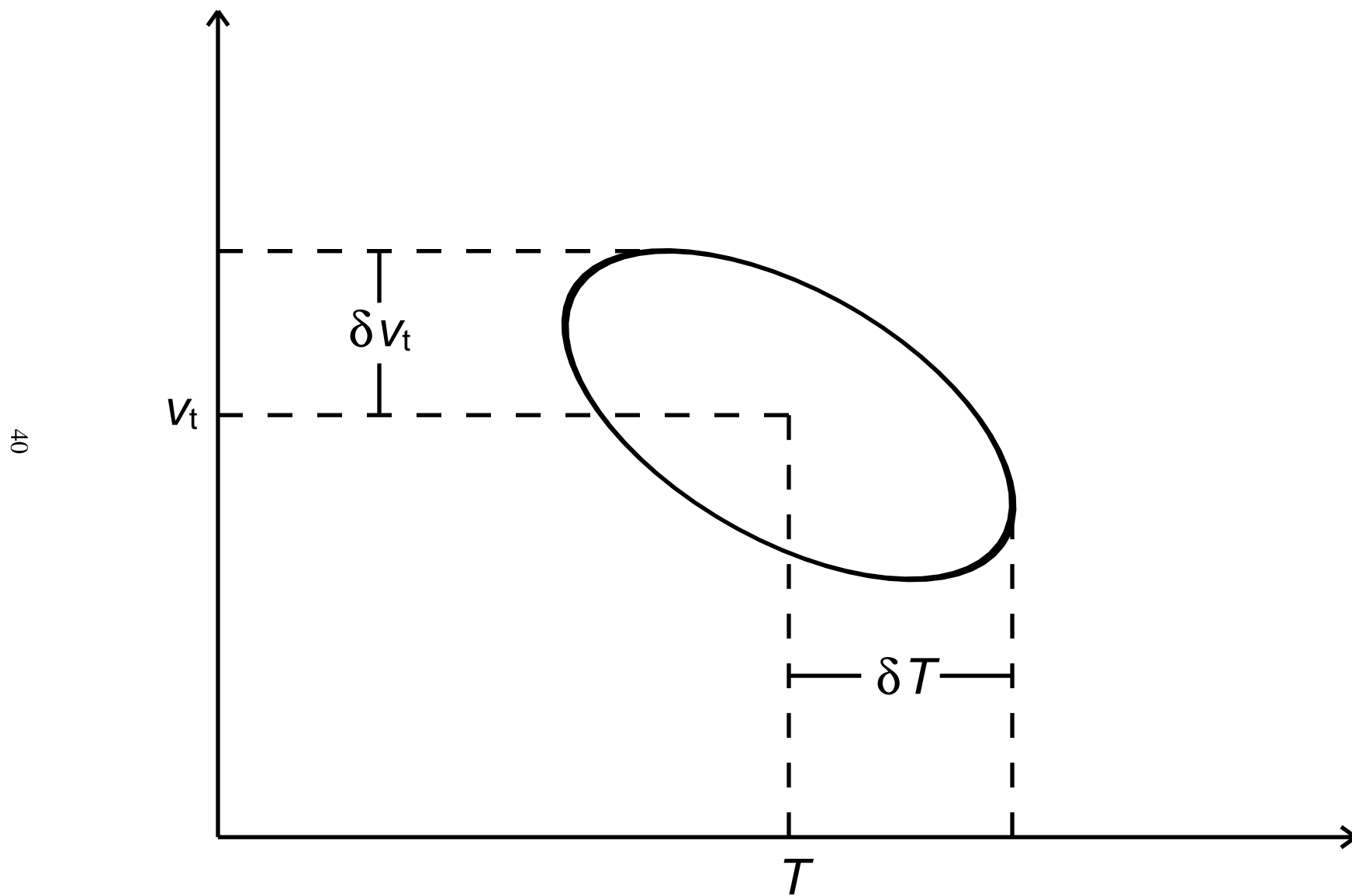


Figure 3



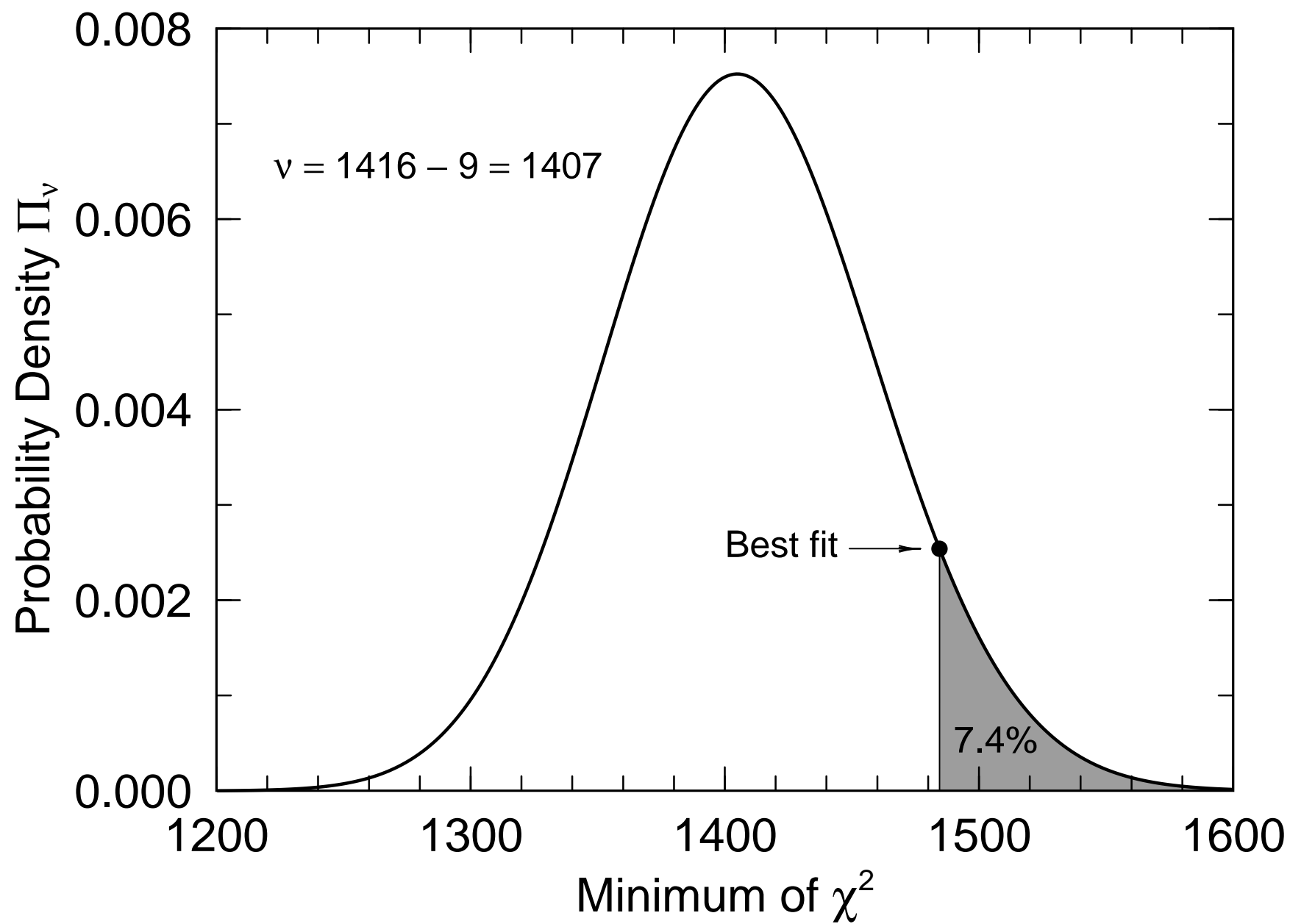


Figure 4

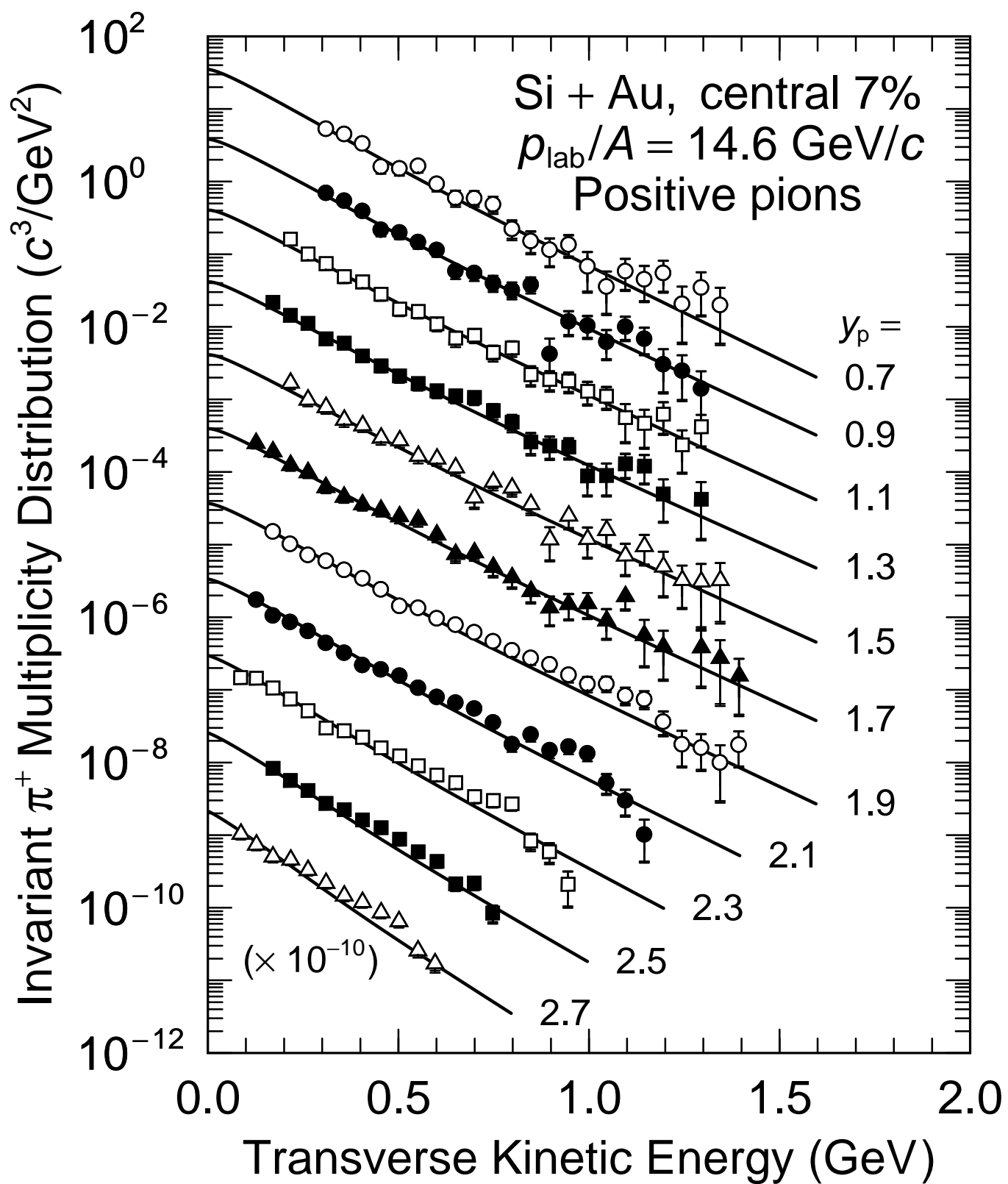


Figure 5

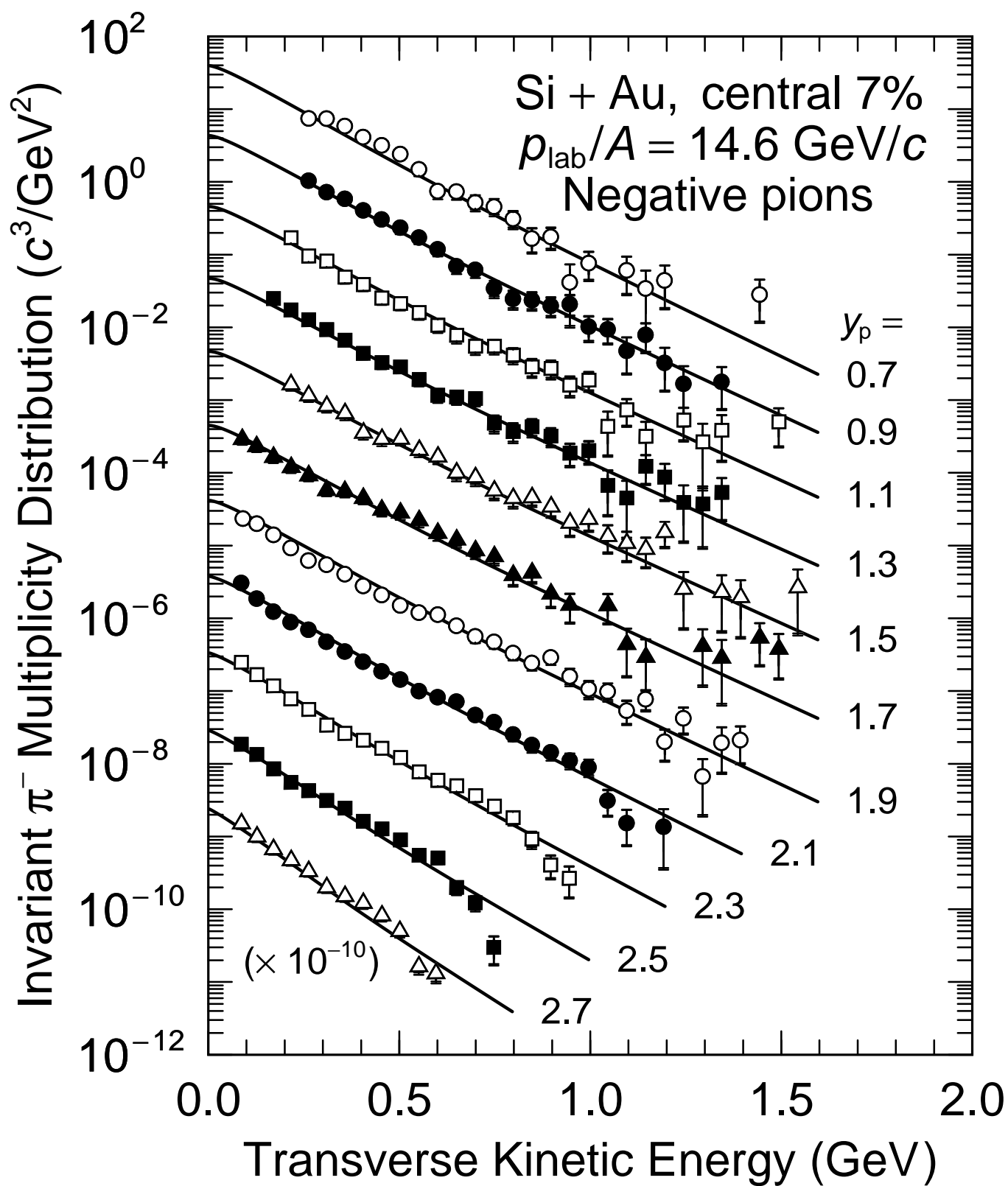


Figure 6

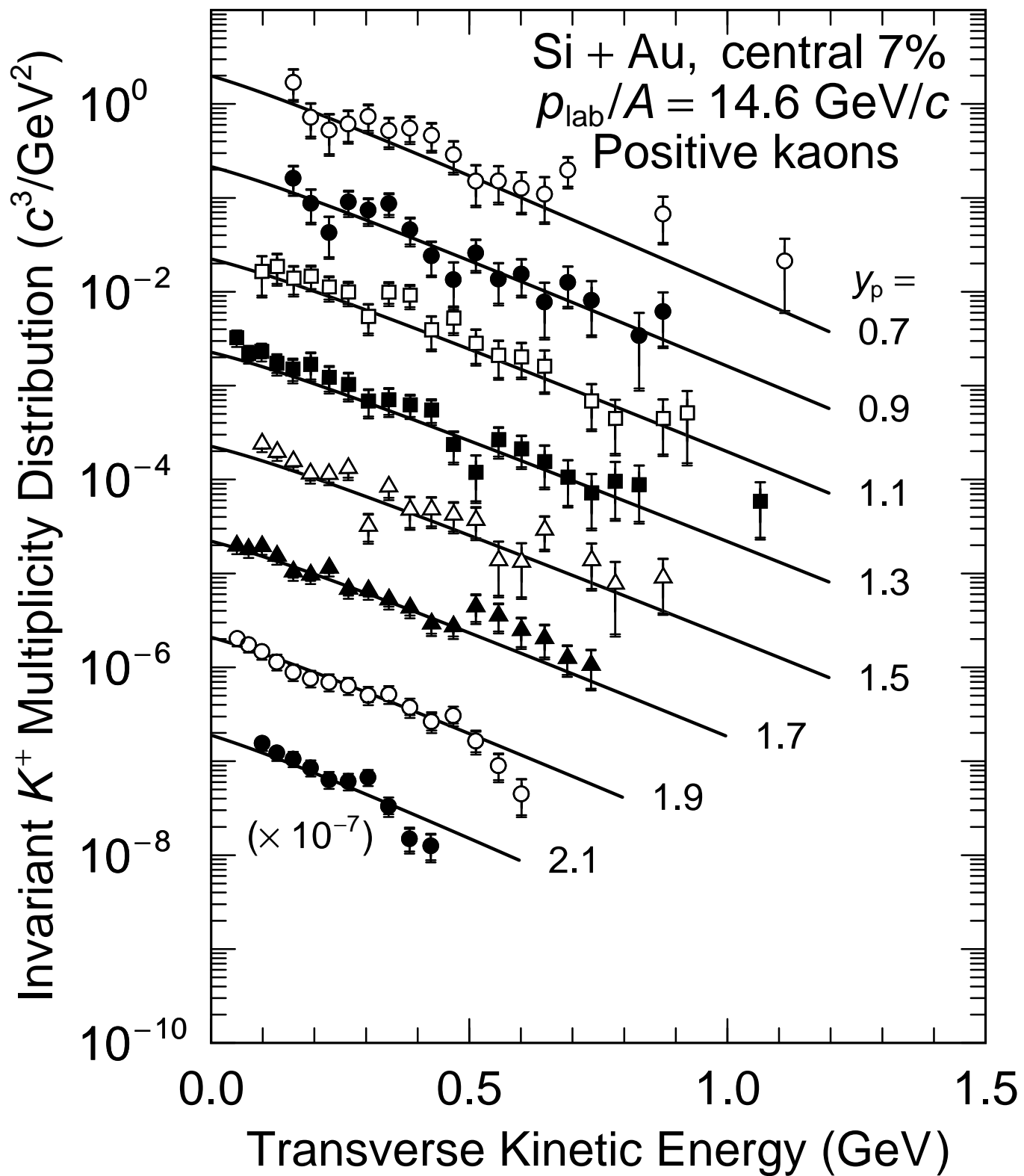


Figure 7

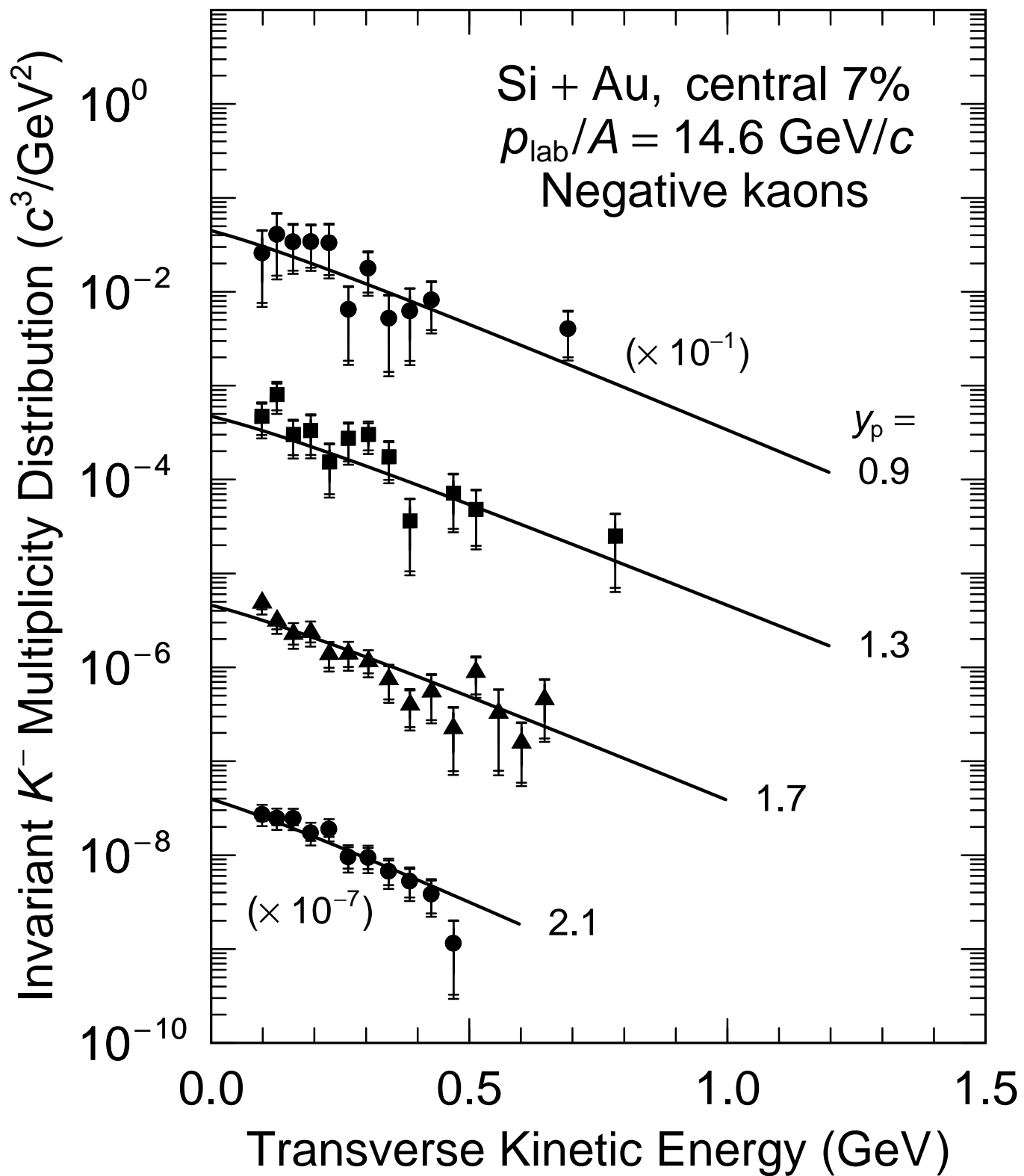


Figure 8

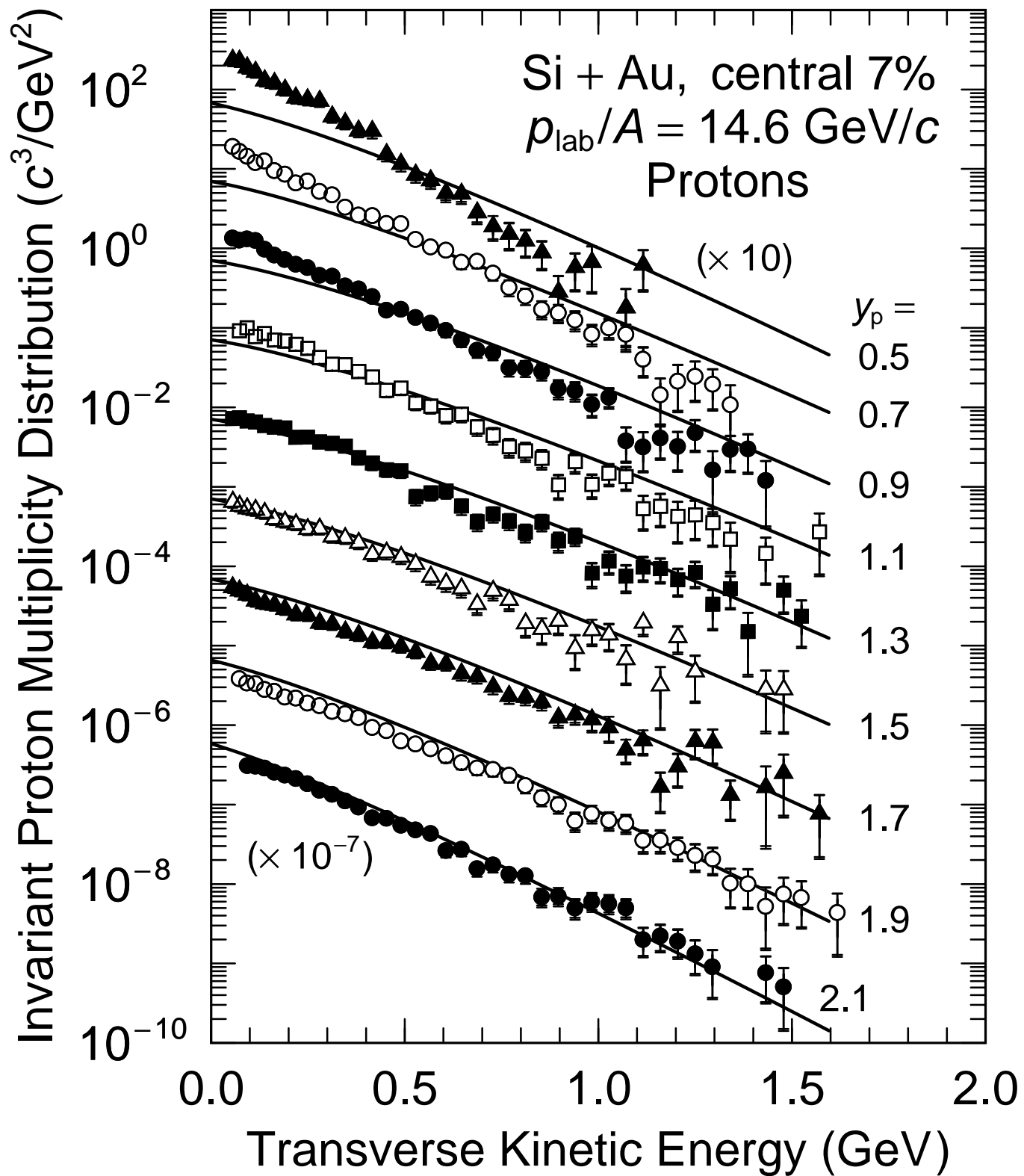


Figure 9

$Y = 1.5$   
 $K_t = 400 \text{ MeV}/c$   
 $q_{\text{side}} = 0$

Si + Au, central 7%  
 $p_{\text{lab}}/A = 14.6 \text{ GeV}/c$   
 Positive pions

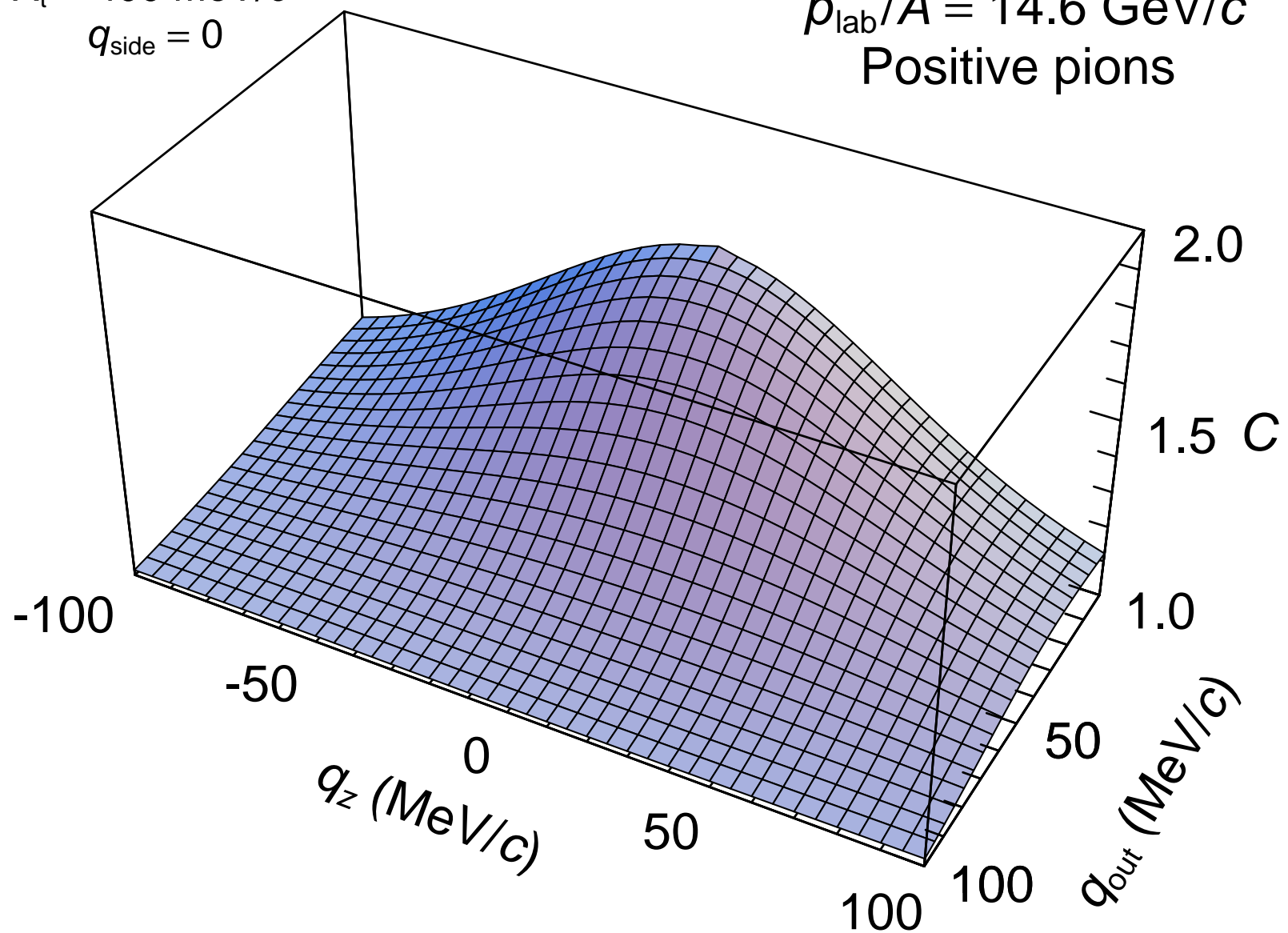


Figure 10

$Y = 1.5$   
 $K_t = 500 \text{ MeV}/c$   
 $q_{\text{side}} = 0$

Si + Au, central 7%  
 $p_{\text{lab}}/A = 14.6 \text{ GeV}/c$   
 Positive kaons

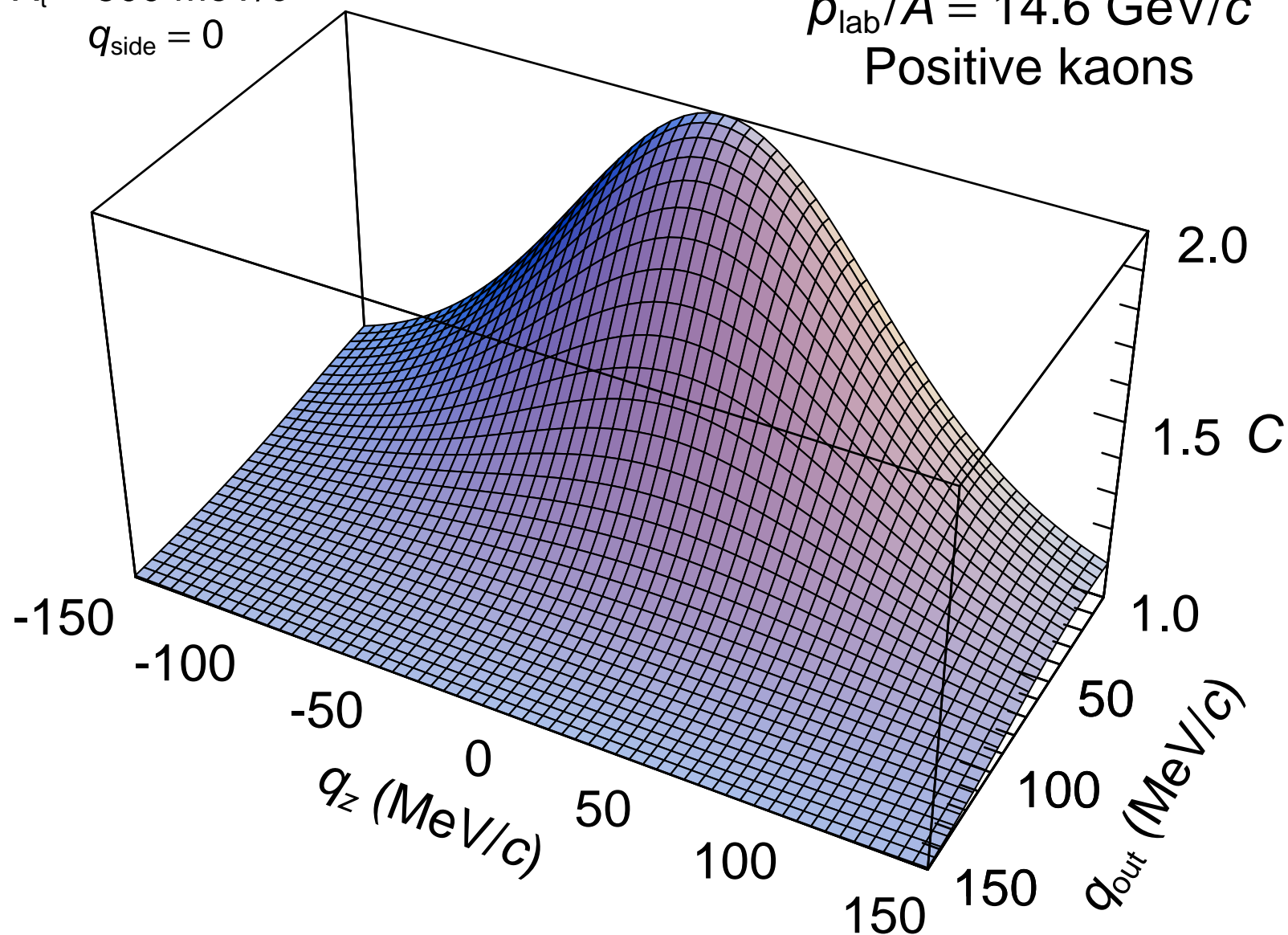


Figure 11



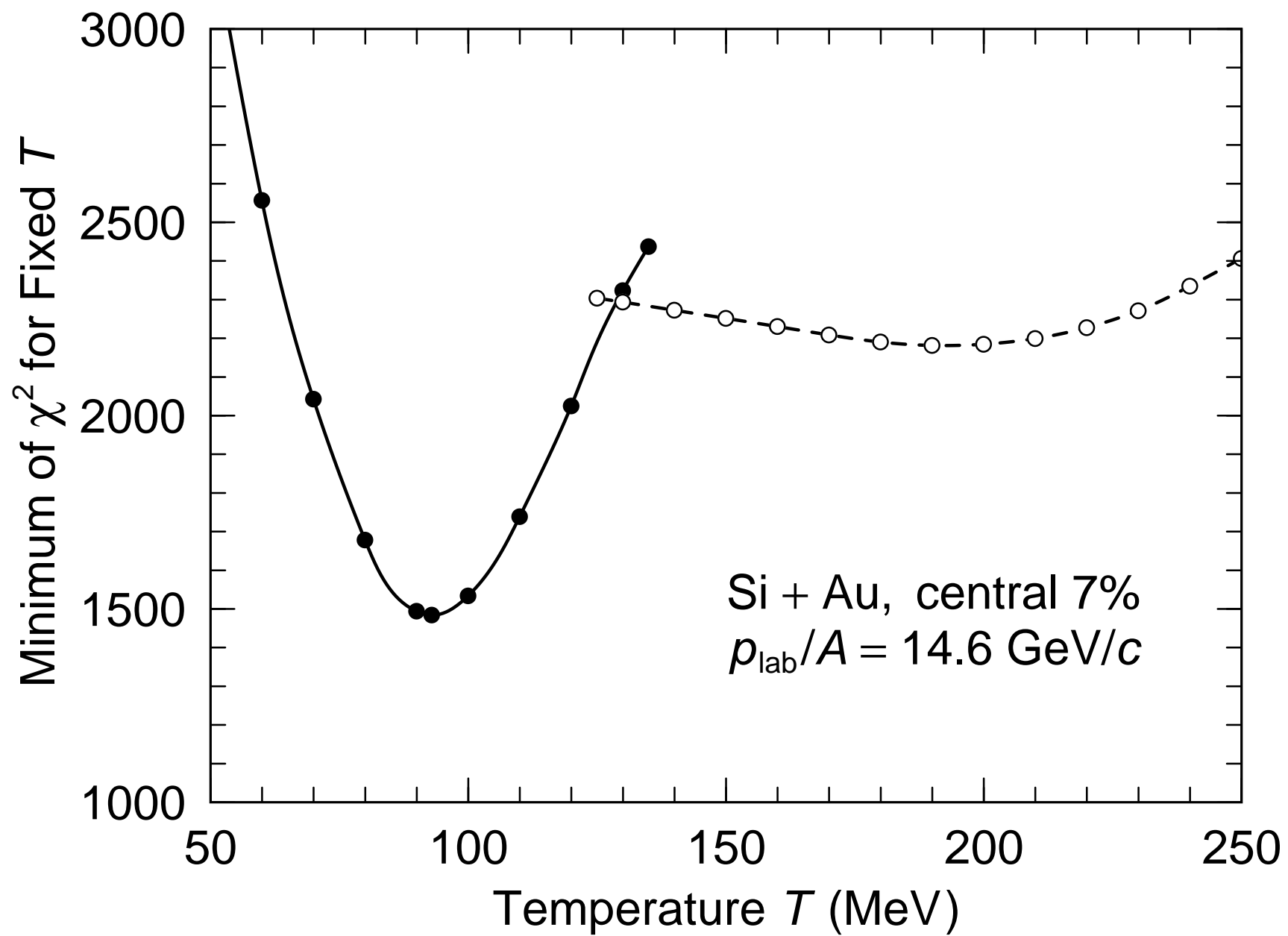


Figure 12